Accelerated methane storage in clathrate hydrates using mesoporous (Organo-) silica materials

Accelerated Methane Storage in Clathrate Hydrates Using Mesoporous (Organo-) Silica Materials

Nithin B. Kummamurum[1,], Geert Watson[2], Radu-George Ciocarlan[3], Sammy W. Verbruggen[1,4], Pegie Cool[3], Pascal Van Der Voort[2], Patrice Perreault[5,6]*

[1]Sustainable Energy Air & Water Technology (DuEL), Department of Bioscience Engineering, University of Antwerp, Groenenborgerlaan 171, 2020 Antwerpen, Belgium.

[2]Centre for Ordered Materials, Organometallics and Catalysis (COMOC), Department of Chemistry, Ghent University, Krijgslaan 281-S3, 9000 Ghent, Belgium.

[3]Laboratory of Adsorption and Catalysis, Department of Chemistry, University of Antwerp, Universiteitsplein 1, 2610 Wilrijk, Belgium.

[4]NANOlab Center of Excellence, University of Antwerp, Groenenborgerlaan 171, 2020 Antwerpen, Belgium.

[5]Faculty of Science, Instituut voor Milieu & Duurzame Ontwikkeling (IMDO), Campus Groenenborger – Building V.612, Groenenborgerlaan 171, 2020 Antwerpen, Belgium.

[6]University of Antwerp, BlueApp, Olieweg 97, 2020 Antwerpen, Belgium.

Nithin B. Kummamuru and Geert Watson contributed equally to this work.

ABSTRACT

Methane (CH_4) clathrate hydrates have gained much attention in the ever-growing search for novel energy storage methods; however, they are currently limited due to their poor water-to-hydrate conversions and slow formation kinetics. To surmount these bottlenecks, significant research has been centered on the design of novel methods (porous media). In this vein, the present work explores two hydrophobic mesoporous solids, an alkyl-grafted mesoporous silica (SBA-15 C8) and a periodic mesoporous organosilica (Ring-PMO), in their ability to promote CH_4 clathrates. Both materials have shown to facilitate CH_4 clathrate formation at mild operating conditions (6 MPa and 269 K to 276 K). The study revealed that the maximal CH_4 storage capacities are strongly linked to the critical/optimal quantity of water in the system which was determined to be at 130% and 200% of the pore volume for SBA-15 C8 and Ring-PMO, respectively. Up to 90% and 95% of the maximum water-to-hydrate conversions were achieved in 90 min at the lowest experimental temperature and critical water content for SBA-15 C8 and Ring-PMO, respectively. At these conditions, SBA-15 C8 and Ring-PMO showed a maximum gas uptake of 98.2 and 101.2 mmol CH_4/mol H_2O, respectively. Both the materials exhibited no chemical or morphological changes post-clathrate formations (characterized using FT-IR, N_2 sorption, XRD, and TEM), inferring their viability as clathrate promoters for multiple cycles. An integrated multistep model was considered adequate for representing the hydrate crystallization kinetics and fits well with the experimental kinetic data with a low average absolute deviation in water-to-hydrate conversions among the three distinct kinetic models analyzed. Overall, the results from this study demonstrate hydrophobic porous materials as effective promoters of CH_4 clathrates, which could make clathrate-based CH_4 storage and transport technology industrially viable.

KEYWORDS: Methane; clathrate; mesoporous (organo-) silica; kinetics

1. Introduction

The world's energy demand is skyrocketing to bolster the expanding population and the burgeoning economy. Contemporaneously, energy policies and regulations are constantly evolving to emphasize using natural gas and hydrogen (H_2) as crucial requirements for maintaining the environment's security globally[1, 2]. Using natural gas, which has a methane (CH_4) content of over 95% and burns relatively clean compared to coal, could be a viable transition option for meeting the energy demands right now towards a fully sustainable energetic strategy[3]. Consequently, improved technologies for high-density storage and transportation are key to using natural gas to its full potential. The current method for storing gas in a compressed gas phase raises safety concerns due to its high-pressure requirement and the flammable nature of CH_4, additionally, liquifying gas for transportation is an energy-intensive operation, making transportation inefficient[4]. Aside from these commercially available technologies, research on low-cost synthetic porous materials with high chemical, mechanical, and thermal stabilities is actively being developed in pursuit of CH_4 storage via adsorption[5-10]. Alternatively, the usage of gas hydrates is a novel and intriguing alternative technology that has received significant attention for high-density CH_4 storage and transportation[11-13].

Gas hydrates or clathrates are crystalline compounds that potentially form at high pressures and low temperatures when non-polar gases are trapped within solid water (H_2O) lattice (polyhedral cavities), where a unit volume of hydrate can deliver approximately ca. 160 m^3 of CH_4 at standard conditions[14]. This substantial increase in energy density can highlight that CH_4 hydrate or clathrate could be an economically advantageous alternative storage technology. However, the commercialization of hydrate technology is stymied by several challenges and is not yet industrially competitive with conventional storage and transport technologies owing to its poor water-to-hydrate conversions and slow kinetics caused by

inadequate mass transfer between hydrate forming gas/H_2O and inefficient removal of hydration heat that does not promote hydrate growth[15, 16]. Enhancement of mass and hydration heat transfer has been the subject of extensive research using various approaches such as reactor design (stirred tanks[17-22], spray nozzles[23-26], bubble columns([27, 28]), kinetic/thermodynamic promoters (sodium dodecyl sulfate (SDS)[29-31], $SC_{12}S$[32], and tetrahydrofuran (THF)[33-35]). However, these approaches also possess certain limitations that preclude achieving high-density storage[36]. A comprehensive review and list of kinetic/thermodynamic promoters for CH_4 hydrates are presented by Nasir et al.[37] and Kummamuru et al.[36], respectively.

Besides reactor designs and promoters, continuous research efforts[38-40] have demonstrated that synthetic porous materials (in fixed-bed columns) can accelerate the kinetics of hydrate formation and water-to-hydrate conversion and the current research is progressing in investigating such potential porous materials with some of the actively pursued materials being silica-based materials [41-60], carbon-based materials[61-76], metal-organic frameworks[77-84], zeolites[85-88], glass beads[60, 89-92], interstitial space between stainless steel beads/fiber[93-95], aluminum foam[96, 97] and silicon carbide[98]. Multiple variables, particularly, pore confinement, gas saturation at the interface, and surface wettability, all of which are influenced by surface chemistry, pore size, and geometry, play an important role in CH_4 hydrate formation and kinetics. Recent studies have shown that hydrophobic materials are more efficient than hydrophilic materials at enhancing hydrate nucleation and growth[44, 61, 83, 92, 99-104]. Although hydrophobic pores seldom adsorb H_2O, sudden adsorption of H_2O was seen in these nanopores above P/P^0 (relative pressure) of 0.5, depending on surface functional groups and pore diameters[62, 105-107]. It was also reported that H_2O can be adsorbed and stabilized in hydrophobic pores free from surface functional groups by cluster formation[108-110]. In addition, thermodynamic studies show that H_2O molecules prefer to

minimize their free energy by clustering as they encounter difficulties in forming hydrogen bonds with hydrophobic surfaces[50, 61, 111, 112]. From these investigations, it can also be deduced that, unlike H_2O bonding with hydrophilic surfaces, the hydrophobic materials tend to have poor H_2O bonding with their surfaces, which enhances H_2O mobility and can promote hydrate nucleation. Molecular simulations by Nguyen et al.[113] also showed enhanced local gas density at the hydrophobic surface and the clustering mechanism of H_2O facilitating hydrate formation. Analogous research by Iiyama et al.[114] and Li et al.[115] using XRD and Raman spectroscopy also corroborated these findings. Studies from Casco et al.[62] have shown that hydrophobic properties of activated carbon can boost CH_4 hydrate growth and similar research by Wang et al.[50] showed that the induction time in hydrophobic sands was at least 8 times shorter than in hydrophilic sands for CH_4 hydrate formation. Hydrophobisized fumed silica nanoparticles, on the other hand, demonstrated good promoting effects on CH_4 hydrate formation[48, 49]. Mileo et al.[116] in their recent molecular simulation study also explored the stability of CH_4 hydrates in different hydrophobic linkers grafted to silica-based materials and concluded that a certain degree of hydrophobic linkers coupled with larger pore sizes are beneficial for stabilizing the clathrate phase at 6 MPa and 260 K.

Considering the potential of hydrophobicity in promoting gas hydrate formation, it is imperative to develop/design and investigate such a porous material to attain a maximum CH_4 storage capacity for large-scale industrial applications. In contrast to the conventional low-dimensional pore sizes and networks in activated carbons, this study focuses on well-defined pore structures of alkyl-grafted mesoporous silica and periodic mesoporous organosilica having pore diameters approximately 6 times greater than the sI unit cell (1.2 nm) of CH_4 hydrate[14]. Due to the sheer influence of hydrophobic pores on H_2O activity, this relatively large confined space can offer an interfacial area for CH_4 hydrate formation and also contributes to promoting hydrate growth. Although both materials share similar chemical characteristics,

they fundamentally differ in the architecture of their pore shape, network, and size. Concurrently, limited research is available in the literature[76, 117, 118] exploring the effects of pore size and network on CH_4 hydrate nucleation and water-to-hydrate conversion. In light of this, the current study aims to enhance the understanding of how the mesoporous structures of alkyl-grafted mesoporous silica, hereafter referred to as (SBA-15 C8) and periodic mesoporous organosilica, hereafter referred to as (Ring-PMO), affect CH_4 hydrate nucleation/formation/growth at 269 K, 274 K, 276 K and an initial pressure of 6 MPa with multiple pore volume-H_2O saturations. As a result, the kinetics of CH_4 hydrate formation, as well as the effects of H_2O content on gas uptake, and water-to-hydrate conversions are also investigated.

2. Experimental methods

2.1. Materials

The chemicals used in this work are listed in Table 1 and were used without any additional purification.

2.2. Synthesis and characterization methods

Mesoporous silica, SBA-15, was synthesized according to a classical procedure, already reported in the literature[119]. The surfactant templated synthesis involved the use of P123 as a structure-directing agent. In the first step, 4.07 g P-123 (0.7 mmol) was dissolved in a 1.68 M HCl solution containing 144.13 ml H_2O (8 mmol) and 20.17 ml $HCl_{(aq,\ 37\%)}$ (242 mmol), after which 9.12 ml the Si-source (41.2 mmol), in the form of namely tetraethyl orthosilicate (TEOS), was added and the whole mixture was stirred for 7.5 h at 318 K. Next, the white precipitate was aged overnight at 353 K, under static conditions. Subsequently, the white

100 precipitate was filtered and washed with distilled H_2O, dried (333.2 K), and calcined at 823 K
101 for 6 h (1 K/min.), resulting in the pristine SBA-15 material.
102 In order to alter the hydrophilic-hydrophobic properties of the SBA-15, a post-synthesis
103 approach was employed. In the first step, 5 g of SBA-15 were dried for 3 h at 473 K and mixed
104 with 150 mL of toluene under an inert atmosphere. After 30 min of stirring, 20 g of
105 trimethoxy(octyl)silane was added and the mixture was stirred for 3 days at 353 K. To remove
106 the unreacted modifier, the precipitate was filtrated and washed 6 times with 70 mL of toluene.
107 Finally, the white powder was dried overnight at 323 K and this product is denoted as SBA-15
108 C8 in what follows.
109 In a general Ring-PMO synthesis, a flask was charged with a 0.96 M HCl solution, containing
110 180 ml H_2O and 14.4 ml (173 mmol) $HCl_{(aq,\ 37\%)}$, to which 35.04 g (470 mmol) KCl and 1.5
111 g (0.26 mmol) P-123 were added. The mixture was left to stir at 318 K until a homogeneous
112 solution with a blue hue was observed. Next, 8.16 ml (20.26 mmol) of HETSCH is added and
113 the whole is continued to stir for 3 h at 318 K. Afterwards, the flask is put in an oven for 24 h
114 at 368 K to complete the organosilica network condensation after which the as-formed white
115 solid is collected through vacuum-assisted filtration. Unreacted silanes and surfactants are
116 removed through extensive Soxhlet extraction using acetone. Residually bound solvent
117 molecules are removed from the porous solids through an activation step where the materials
118 are subjected to reduced pressures (≤ 5E-4 MPa) at temperatures of 393 K. The yield of the
119 Ring-PMO synthesis was found to be virtually quantitative. A chemical representation of Ring-
120 PMO and SBA-15 C8 is presented in Figure 1.
121 Two-dimensional transmission electron microscopy (2D TEM) pictures were taken using a
122 JEOL JEM-1010 TEM instrument operated at 100kV without spherical aberration (Cs)
123 correction. The powder X-ray diffraction (PXRD) pattern was measured with a Bruker D8
124 Advance with autochanger using Cu K-alpha irradiation with a wavelength (λ) of 0.154 nm in

125 a Bragg-Brentano geometry. PXRD diffractograms were determined in the range of 0.2-10°
126 with a step-size of 0.015°. The porosity of the materials was assessed through N_2-sorption, as
127 performed on a Quantachrome Quadrasorb automated sorption system operated at 77 K. Prior
128 to the analyses, the samples were degassed at 393 K for 16 h. A Nicolet 6700 Fourier Transform
129 IR (FT-IR) spectrometer was used to perform in-situ diffuse reflectance infrared FT (DRIFT)
130 measurements. The samples were heated to 393 K, under vacuum, for 20 min and this
131 temperature was maintained during the spectra acquisitions. The samples were diluted in KBr
132 (2 wt.%), and 100 scans were accumulated for each spectrum with a resolution of 4 cm^{-1} in the
133 region of 4000–500 cm^{-1}. Quantification of the C8 density of the SBA-15 C8 material was
134 performed through TGA analysis using a Mettler Toledo TGA/DSC 3+ star system. The
135 obtained TGA results were corroborated with the N_2-sorption analysis (BET surface area), to
136 approximate the surface functional group density of the C8 molecule. For this, the mass loss
137 considered in the TGA-profile analysis was between 473 K and 1073 K, assuming that the
138 toluene, which was used as a solvent and washing agent during the post-synthesis modification
139 protocol, evaporates below this temperature.
140
141 2.3. Experimental apparatus and procedure
142 As seen from the schematic layout (Figure 2), CH_4 hydrate formation tests were conducted
143 in stainless steel cylindrical reactor (effective volume: 150 cm^3) purchased from Swagelok
144 (316L-50DF4-150) which can withstand gas pressures up to 34.4 MPa. The reactor was
145 immersed in a high-precision circulating bath (CORIO CP-1000F, JULABO GmbH) filled with
146 a water-ethylene glycol mixture to maintain the cold and stable temperature inside the reactor.
147 The temperature stability of the bath was ± 0.03 K. The pressure in the reactor was measured
148 for every 1 Hz, using a pressure transmitter (PAA3X-30 MPa; KELLER AG für

149 Druckmesstechnik; a range of 0-30 MPa absolute, with ± 0.01% FS accuracy). The methane
150 gas (99.99% purity) used in this study was supplied by Air Liquide Benelux Industries.
151 A standard method was employed to investigate the CH_4 hydrate formation and the
152 experimental procedure is described as follows. Prior to the commencement of experiments,
153 the reactor was cleaned with H_2O and dried, followed by adding 1 g of synthesized material
154 (dried at 343 K overnight) and a certain volume of deionized H_2O based on the required level
155 of pore volume saturation. Subsequently, the atmospheric gases in the reactor were flushed by
156 purging CH_4 gas at 0.2 MPa at least 10 times. Then, the reactor was submerged in the water-
157 ethylene glycol bath i.e. maintained at 303 K, and CH_4 gas pressure was gradually increased to
158 6 MPa. These steady ambient conditions were opted to hinder any hydrate formation. Upon
159 stabilizing the system under these conditions (303 K and 6 MPa), the reactor was cooled to the
160 experimental temperature for initiating the hydrate formation. The hydrate conversion is
161 deemed completed when no significant pressure drop (0.02 MPa in 30 min) was observed. Each
162 experiment in this study was repeated two times.
163 The amount of CH_4 gas consumed during hydrate formation was estimated using the
164 compressibility factor equation of state as shown in (Eq. 1), the normalized gas uptake (NG_t,
165 Hydrate growth) at any given time t is calculated using (Eq. 2), The percentage of H_2O to
166 hydrate conversion is determined by (Eq. 3)
167

$$\Delta n_{hyd,t} = V_r \left[\left(\frac{P}{zRT} \right)_{t=0} - \left(\frac{P}{zRT} \right)_t \right] \quad \text{(Eq. 1)}$$

168

$$NG_t = \frac{\Delta n_{hyd,t}}{n_{H2O}} \; (moles\ of CH_4 \,/\, moles\ of H_2O) \quad \text{(Eq. 2)}$$

169

$$WtH(\%) = \frac{\Delta n_{hyd,t} \times Hn}{n_{H2O}} \times 100 \quad \text{(Eq. 3)}$$

where, $\Delta n_{hyd,t}$ is the moles of CH_4 gas consumed at time *t*; V_r is the gas-phase volume within the reactor measured using the helium expansion method[93, 120]; *R* is the ideal gas constant; *T* and *P* are the temperature and pressure within the reactor; *z* is the compressibility of gas calculated using the Pitzer correlation[121]; n_{H2O} in (Eq. 2) is the number of moles of H_2O introduced into the reactor and Hn in (Eq. 3) refers to the hydration number which is defined as the number of H_2O molecules required to encapsulate one guest (CH_4) molecule and an ideal hydration number of 5.75 is adapted in this work to comply with other CH_4 hydrate experiments available in the literature[93, 122].

The gas storage capabilities of porous materials were evaluated based on CH_4 capacity relative to the sample's H_2O content (hydrate storage capacity: q^w_{CH4}), and CH_4 capacity relative to the dry mass of the solid (dry weight storage capacity: q^A_{CH4}) as shown in (Eq. 4) and (Eq. 5)

$$q^w_{CH4}(wt.\%) = \frac{m_{CH4}}{(m_{H2O} + m_{CH4})} \times 100 \quad \text{(Eq. 4)}$$

$$q^A_{CH4}(wt.\%) = \frac{m_{CH4}}{(m_{solid} + m_{CH4})} \times 100 \quad \text{(Eq. 5)}$$

Here, m_{H2O} and m_{solid} denote the masses of the H_2O and dried solid in the reactor, while m_{CH4} denotes the quantity of enclathrated CH_4 as calculated from (Eq. 1).

Furthermore, another essential representation for industrial application purposes is the CH_4 capacity relative to the total mass of the system (total weight storage capacity: q^T_{CH4}), which was also evaluated as shown in (Eq. 6)

$$q^T_{CH4}(wt.\%) = \frac{m_{CH4}}{m_{tot}} \times 100 \quad \text{(Eq. 6)}$$

Here, m_{tot} refers to the mass of the total system, taking into account the mass of the dried solid, the H_2O, as well as the enclathrated CH_4.

189 The rate of CH_4 hydrate formation is calculated using a discrete first-order forward difference
190 method as shown in (Eq. 7).

$$\frac{dN_t}{dt} = \left(\frac{d\Delta n_{hyd}}{dt}\right) = \frac{\Delta n_{hyd,t+\Delta t} - \Delta n_{hyd,t}}{\Delta t}, \Delta t = 0.5\ min \quad \text{(Eq. 7)}$$

191

192 3. CH_4 Hydrate kinetics

193 One of the methods for analyzing the hydrate growth is by evaluating the post-induction time
194 data using different reaction models. In this work, the CH_4 uptake upon hydrate formation was
195 studied under isothermal conditions, and the kinetics of hydrate growth (enclathration reaction)
196 in the presence of porous media was analyzed with three different kinetic models. The
197 crystallization kinetics of gas hydrates can be adequately explained utilizing the Johnson-Mehl-
198 Avrami-Kolmogorow (JMAK) [123-125] model, which assumes the kinetics of isothermal
199 phase transformation from H_2O/guest gas (CH_4 in this work) to solid-state based on random
200 nucleation with a constant growth rate. This model has previously been applied to investigate
201 hydrate growth kinetics[122, 126-131] and is presented in (Eq. 8)

$$\alpha_{WtH} = 1 - \exp\left(-k(t)^n\right) \quad \text{(Eq. 8)}$$

202

203 where, α_{WtH} is water-to-hydrate conversion ratio at time t, k, and n are
204 formation/crystallization rate constant and Avrami exponent respectively, which can be
205 obtained by fitting the experimental data.

206 In addition to the JMAK model[125], Lee et al.[132] proposed a kinetic model with two
207 adjustable parameters to investigate hydrate growth in porous media, and the amount of gas
208 consumed during hydrate formation is described as a function of time (Eq. 9)

$$\frac{n_{gas}}{n_{H2O}} = \frac{\alpha}{5.75}\left[1 - \exp\left(-5.75K\left(f_{exp} - f_{eq}\right)t\right)\right] \quad \text{(Eq. 9)}$$

where, n_{gas} is the mole of gas consumed during hydrate formation at the time t, n_{H2O} is the mole of H_2O used in the experiment, f_{exp} and f_{eq} are the fugacities of gas in the vapor phase (MPa) at the operating thermodynamic conditions and in three-phase equilibrium (MPa), which are obtained from Holley et .al[133]. K and α are the adjustable parameters where K is regarded as the overall rate constant (min^{-1} MPa^{-1}).

While the JMAK model[125] is often used in the literature, and can adequately describe the initial crystallization of hydrates, it is also important to emphasize that the diffusion of guest gas/H_2O through the hydrate layer is limited or hindered at the latter stage of hydrate growth[134, 135]. Considering this, the hydrate growth kinetics can be described by both primary crystallization and diffusion-controlled secondary crystallization rate by evaluating the experimental data with the reaction model proposed by Hay[136], presented in (Eq. 10)

$$\alpha_{WtH} = \alpha_P(1 - \exp(-k_P t^n))(1 + (k_s t^{0.5})) \quad \text{(Eq. 10)}$$

where, α_{WtH} and α_P are water-to-hydrate conversion ratio at time t, and at the end of the primary process, respectively. k_P and k_s are the rate constant for primary crystallization growth and the rate constant for diffusion-controlled secondary crystallization growth, respectively. n is Avrami exponent. Although the model presented in (Eq. 10) is extensively used in polymer crystallization[136-139], it is for the first time adopted for gas hydrates in our work as the model can fundamentally explain the hydrate initial growth based on the JMAK model[125] (first term in Eq. 10) and later affected by the diffusion (second term in Eq. 10). More details on the analysis are presented in the results and discussion section.

The performance of these kinetic models in predicting water-to-hydrate conversion was quantified using average absolute deviation (AAD) as shown in (Eq. 11),

$$AAD = \frac{1}{N}\sum_{i=1}^{N}|E_i^{\alpha} - P_i^{\alpha}| \quad \text{(Eq. 11)}$$

230 N, E_i^{α} and P_i^{α} refer to the number of data, experimental and predicted water-to-hydrate
231 conversion respectively.
232
233 4. Results and discussion
234 4.1. Material characterizations
235 SBA-15 C8 and Ring-PMO were subjected to multiple characterizations both pre- and post-
236 clathrate formation. The current section presents the characterization of the materials pre-
237 clathrate formation and section 4.5 presents material characterizations post-clathrate formation.
238 The investigation of the FT-IR spectra recorded for both materials, as shown in Figure 3,
239 clearly demonstrates the siliceous nature, owing to the broad band around 3400 cm^{-1}, together
240 with the prominent peaks at 1100 cm^{-1} and 800 cm^{-1}, indicating the presence of -OH groups,
241 Si-O-Si bonds, and Si-OH species respectively. When comparing the FTIR spectra of pure
242 SBA-15 and the alkyl-chain grafted SBA-15 C8 (Figure S1), a substantial reduction in the Si-
243 OH band at 3750 cm^{-1}, as well as the emergence of bands at 2800-3000 cm^{-1}, indicates the
244 successful surface modifications with C8 chains. The identical bands at 2800-3000 cm^{-1} in the
245 Ring-PMO sample also provide evidence of the organic nature of the PMO material.
246 Upon investigation of the TGA curve, as recorded for the SBA-15 C8 sample (Figure S2),
247 further confirmation of the successful alkyl grafting was concluded. A mass loss of 15.39%
248 between 473 K and 1073 K was observed, originating from the degradation of the surface octyl
249 groups. The grafting density of the C8 chains, expressed in groups per nm^2, is subsequently
250 calculated using (Eq. 12)
251

$$Grafting\ density\ \left(\frac{groups}{nm^2}\right) = \frac{\Delta m \times N_A}{M_{group} \times S_{BET}} \qquad \text{(Eq. 12)}$$

252 where Δm is the weight loss as determined using the TGA curve, N_A is Avogadro's constant,
253 M_{group} is the molar mass of the octyl chain and S_{BET} is the surface area of the SBA-15 material

254 before the surface modification. Ultimately it was determined that the SBA-15 C8 material has
255 a grafting density of ≈ 1.2 octyl groups per nm^2.

256 As shown in Figure 4a, both SBA-15 and SBA-15 C8 materials, as well as Ring-PMO
257 material, exhibit type-IV isotherms with H1 hysteresis which is an archetypical of mesoporous
258 materials with cylindrical pores. Pore size analysis using the BJH methods further confirms the
259 presence of mesoporous in the range of 5 nm and 8 nm for the SBA-15 and Ring-PMO
260 materials respectively (Figure 4b). The Nitrogen uptake at $P/P° > 0.95$ for the SBA-15 samples
261 is due to interparticle porosity and is not taken into account in the pore size distribution. For
262 the Ring-PMO there is even a larger nitrogen uptake at $P/P° > 0.95$. Next to possible
263 interparticle porosity, the Ring-PMO possesses also – next to the hexagonal mesoporous –
264 larger spherical voids (See TEM image in Figure 6c). Uptake at relative pressures in the region
265 $P/P° = [0.95, 0.99]$ corresponds to voids of 20 - 100 nm. While a high BET surface area of 676
266 $m^2\ g^{-1}$ was observed in the case of pure SBA-15, the surface area decreased to 345 $m^2\ g^{-1}$ upon
267 surface grafting of the C8 chains. The aforementioned surface modification also resulted in a
268 decrease from 0.78 $cm^3\ g^{-1}$ to 0.49 $cm^3\ g^{-1}$ in total pore volumes. The Ring-PMO material also
269 exhibited high surface area and total pore volume of 849 $m^2\ g^{-1}$ and 0.99 $cm^3\ g^{-1}$. Table 2
270 outlines the properties of the hydrophobic porous materials used in this work.

271 Information on the structural ordering of the materials was determined using XRD and the
272 data is shown in Figure 5. The diffractogram of the SBA-15 C8 material exhibit typical (100),
273 (110), and (200) reflections, confirming the archetypical P6mm symmetry of the hexagonally
274 packed mesopores within the structures. In the case of Ring-PMO a single, slightly broader
275 (100) reflection was observed, indicating a less semi-crystalline ordering compared to the SBA-
276 15 C8 sample.

277 The materials were also analyzed through TEM to further investigate the particle
278 morphologies, as well as porosities. As can be seen from Figures 6(a) and 6(b), the SBA-15 C8

material is composed of rod-like particles, with mesopores present throughout the material. The same presence of mesopores in the Ring-PMO material is also confirmed in the TEM images (Figures 6(c) and 6(d)). In Figure 6(c) the spherical voids responsible for the increased nitrogen uptake at high P/P°, as discussed above, can be seen. The mesoporous visible in Figure 6(d) are open and not cubic or inkbottle pores, as the isotherm in Figure 3(a) did not show the typical cavitation at P/P° = 0.42, typical for cubic or inkbottle pores.

4.2. CH_4 consumption and hydrate formation rate

CH_4 hydrate formation experiments were conducted at three different temperatures of 269 K, 274 K, and 276 K at an initial pressure of 6 MPa. Multiple pore-volume saturations ranging from 70% to 350% were chosen to alter the H_2O content in SBA-15 C8 and Ring-PMO, which also meets under-saturated/saturated/over-saturation conditions. To ensure consistency, 1 g of SBA-15 C8 and Ring-PMO was used in all the experiments. Table 3. summarizes the experimental conditions, as well as CH_4 hydrate formation results for SBA-15 C8 and Ring-PMO. Given that a larger driving force has a favorable correlation with both rate of hydrate formation and induction time (shorter), this works sets the experimental pressure of 6 MPa. Accordingly, the calculated driving force is ≈ 3.7 MPa, 3.2 MPa, and 2.7 MPa at 269 K, 274 K, and 276 K, respectively, where the equilibrium pressure for CH_4 hydrate is considered as ≈ 2.3 MPa, 2.8 MPa, and 3.3 MPa at 269 K, 274 K, and 276 K, respectively[36, 140].

Figures 7(a) and 7(b) show the normalized gas uptake during CH_4 hydrate formation in SBA-15 C8 at 269 K and 274 K with multiple pore-volume saturations, respectively. Figures S3, S4, and S5 show the full-time scale of the experiments at 269 K, 274 K, and 276 K. The hydrate formation being exothermic, a sudden spike in the sample bed temperature (measured by K-type thermocouple; Testo SE & Co. KGaA) was considered to be the onset of hydrate formation, where the pressure drop observed within the reactor was translated to CH_4 uptake.

The time zero in all the Figures corresponds to the onset of hydrate formation/nucleation. As seen in Figures 7 and S4, the CH_4 hydrate formation kinetics in SBA-15 C8 at all the experimental conditions are rapid, where approximately 80% to 90% of the gas uptake occurred within 90 min from nucleation. A bar graph of average storage capacities achieved at 90^{th} min is presented in Figure S6. The effect of pore-volume saturation can also be seen in Figure 7 where an increase in H_2O content led to an increase in gas uptake, however, when SBA-15 C8 was saturated with 200% of pore-volume which corresponds to 1 g H_2O, showed a reduced gas uptake compared to 130% pore-volume saturation (0.65 g H_2O). At 269 K and 274 K, a maximum uptake of 82.9 mmol CH_4/mol H_2O and 81.8 mmol CH_4/mol H_2O was observed for 200% pore-volume saturation, which is approximately 15% and 7% lesser than the CH_4 uptake at 130% pore-volume saturation at the respective temperatures. It is plausible that the CH_4 diffusion/circulation pathways through the pore network could be impeded by this relatively high amount of H_2O, which would explain the system's considerable reduction in gas uptake when the H_2O content is higher than the critical value and similar results for optimal H_2O content in carbon materials were also reported by Celzard et al.[70] and Zhou et al.[141]. This shows that there exists an optimum pore-volume saturation for SBA-15 C8 which is considered to be 130%. These experiments reveal the significance of critical H_2O content for high gas storage capacities in porous materials. Furthermore, experiments at 276 K (Figure S5) also showed a similar trend as observed at 269 K and 274 K, with higher gas uptake at 130% pore-volume saturation (73.5 mmol CH_4/mol H_2O) than at 200% pore-volume saturation (72.9 mmol CH_4/mol H_2O). As anticipated, the CH_4 uptake decreased with an increase in temperature from 269 K to 276 K, which indicates the influence of the driving force, and a similar trend was also observed in porous silica gel particles[54]. However, it is also important to mention that the experiments with 70% and 100% pore-volume saturations at 276 K failed to nucleate despite having a driving force of 2.7 MPa.

Figures 8(a) and 8(b) show the average gas uptake during CH_4 hydrate formation at 269 K and 274 K in Ring-PMO with different pore-volume saturations, respectively. Figures S7 and S8 show the full-time scale of experiments at 269 K, and 274 K. Similar to SBA-15 C8, the temperature spikes within the reactor indicated the onset of hydrate formation. In contrast to SBA-15 C8, multiple exothermic peaks within the Ring-PMO bed were observed at the maximum pore-volume saturation used, implying multiple nucleation events and the heterogeneity of hydrate formation and similar observations of multiple temperature spikes in porous materials were also reported in the literature[142-145]. Figure 9 depicts an example of multiple temperature spikes observed in Ring-PMO when saturated to 350% of pore volume. Analogous to SBA-15 C8, Ring-PMO also demonstrated a critical H_2O content for achieving a maximum CH_4 storage capacity, with 101.2 mmol CH_4/mol H_2O when saturated to 200% (2 g H_2O) and 86.7 mmol CH_4/mol H_2O when saturated to 350% (3.5 g H_2O) at 269 K. Despite multiple nucleations, the Ring-PMO at 350% pore-volume saturation showed a lower conversion of H_2O into hydrates and a similar pattern was also seen at higher temperatures (276 K: Figure S9). Akin to SBA-15 C8, the Ring-PMO failed to nucleate at lower pore-volume saturation of 70% at 274 K and from 70% to 130% pore-volume saturations at 276 K. A maximum duration of 6 hrs. was set for any event of hydrate nucleation or temperature spike within the bed, after which the experiments were discontinued. Figure S6 presents a bar graph of storage capacities achieved at 90^{th} min in Ring-PMO at all studied conditions.

The average rate of hydrate formation was measured every 0.5 min from the onset of the nucleation point for both SBA-15 C8 and Ring-PMO at all the conditions studied in this work. As can be seen from Figures S10 and S11, the rate of hydrate formation increased with an increase in pore-volume saturation at both temperatures irrespective of the material used. Despite a depreciation in CH_4 uptake, the 200% pore-volume saturation in SBA-15 C8 at 274 K (Figure S10b) and 276 K (Figure S12) showed a steeper peak compared to 130% pore-

volume saturation owing to its relatively high initial gas uptake upon the nucleation event. Rapid hydrate growth can also be seen upon hydrate formation at 269 K, and 274 K for 130% and 200% pore-volume saturated samples followed by a gradual decrease. Similar results were also observed when the temperature was increased by 2 K but at a slower growth rate. On the other hand, the 350% pore-volume saturation in Ring-PMO (Figure S11) at both temperatures showed a lower rate of hydrate formation compared to 200% pore-volume saturation by virtue of its slow gas uptake which is evident from Figure 8. Multiple nucleation events in 350% pore-volume saturation can also be seen in Figures S11 and S13 if one plots the average rate of gas hydrate formation as a function of time (50 to 300 min). Similar to SBA-15 C8, a rapid hydrate growth was observed in Ring-PMO samples followed by a gradual decrease, however, increasing the temperature to 276 K decelerated the hydrate growth, as a result of driving force.

4.3. Comparison of CH_4 hydrate formation in SBA-15 C8 and Ring-PMO

In order to compare the performance of SBA-15 C8 and Ring-PMO porous materials in promoting CH_4 hydrate formation and growth, their normalized gas uptake curves at 269 K and 274 K are plotted in Figure 10. It is evident from the figure that the CH_4 uptake characteristics of SBA-15 C8 and Ring-PMO are distinctively different even when the driving forces are the same, resulting in a significantly higher gas uptake for SBA-15 C8 compared to Ring-PMO at 70%, 100%, and 130% pore-volume saturations. However, at 200% pore-volume saturation, the Ring-PMO surpassed the storage capacity compared to SBA-15 C8 (c.f. Table 3) at both temperatures, but it is also important to mention that at such a pore-volume saturation the SBA-15 C8 has already demonstrated a drop in gas uptake due to the material's critical H_2O content, as mentioned in the previous section. Similar results were also observed at 276 K (Figure S14). Considering the time taken for experiments to achieve 90% of maximum storage capacity and eventually obtain a plateau, the hydrate formation in SBA-15 C8 was observed to take a longer

period relative to Ring-PMO. For instance, in the case of 130% pore-volume saturation at 274 K, it took approximately 90 min to achieve 90% (47.2 mmol CH_4/mol H_2O) of maximum storage capacity in Ring-PMO (52.4 mmol CH_4/mol H_2O) and 82% (72.2 mmol CH_4/mol H_2O) of maximum storage capacity in SBA-15 C8 (88.0 mmol CH_4/mol H_2O). A summary of water-to-hydrate conversion in SBA-15 C8 and Ring-PMO is tabulated in Table 3 and Figure 11.

As mentioned, optimal clathrate formation conditions differ between the two materials, owing primarily to the amount of H_2O introduced to the system. Nevertheless, it is also important to compare the CH_4 storage capacities on a weight basis for both materials more closely, as shown in Table 4. Standardizing the amount of H_2O in the system revealed that Ring-PMO can store ≈ 1.2 times more CH_4 than SBA-15 C8, furthermore, it can enclathrate up to ≈ 3.2 times more CH_4 per gram of dry material than SBA-15 C8. Although both the materials demonstrated a quick propensity in storing CH_4 as clathrate hydrates, Ring-PMO showed relatively high storage capacity as it can incorporate considerably more H_2O in the reactor, which translates into substantially increased total dry weight storage capacities. Conclusively, the Ring-PMO has a significantly higher total storage capacity than SBA-15 C8 by a ratio of ≈ 2.0 which is of vital importance for future industrial applications.

Attempting to compare the performance of porous materials used in this study with other solid CH_4 hydrate promoters could be of potential interest. However, comparing the absolute values hydrate storage capacity (q_{CH4}^{w}), CH_4 capacity relative to the dry mass of the solid (q_{CH4}^{A}), total weight storage capacity (q_{CH4}^{T}), water-to hydrate conversion, and hydrate growth rate obtained from different laboratories, reactors and methods might not offer the best approach of establishing whether one surpassed the other. For instance, it has been observed[95, 146] that any change in the microstructure (surface roughness) of high-pressure metal reactor will have an immense effect on critical parameters indicated above, and it is also worth noting that the majority of the reactors reported in the literature were made of metal

material. However, it is exemplary to make a comparison of total weight CH_4 storage capacity (q_{CH4}^T) and water loading (R_w: mass of H_2O/mass of solid) as they are essential for industrial application purposes. As shown in Table S1, only works[59, 61, 66, 81, 83, 118, 147-152] using porous materials with $R_w \leq 2.5$ were chosen for comparison with the material that demonstrated higher q_{CH4}^T in this work. As can be observed, there are quite some materials, particularly at low R_w that exhibit better CH_4 storage capacity than that reported in this work; nevertheless, it is worth noting that the experimental pressure employed in their study is higher than the pressure used in this work. On the other hand, it should be emphasized that water loading (R_w) is a significant industrial metric, as cost and mass of solid promoters increases with decrease in R_w. In this regard, it is important to highlight that Ring-PMO from this work is capable of promoting CH_4 hydrate formation at moderate thermodynamic conditions in the mass of water twice its own weight, which could suggest significant cost savings for an industrial application, and this makes the material more appealing than materials that are employed at low water loadings and have higher total storage capacity.

4.4. Kinetic analysis

To investigate the kinetics of hydrate formation at multiple conditions studied in this work, the CH_4 uptake curves were evaluated with different models as described in section 3, and the kinetic analysis was not performed for the materials beyond their critical H_2O content. Figures S15, S16, S17, and S18 show the predicted kinetic curves from the JMAK model[125], and the regressed values of k and n are presented in Table S2. Given the challenges in visualizing hydrate growth morphology in a porous medium, the Avrami kinetic exponent (n) is commonly utilized in interpreting the geometry (growth dimension) of the hydrate formation and the degree of the crystallization process[123, 124, 153]. Where, n = 3 represents the instantaneous three-dimensional growth of a spherical nucleus, n = 2 represents instantaneous two-

dimensional growth, and n = 1 represents one-dimensional growth. But, as shown in Table S2, the regressed exponent values (n) for the entire growth period are less than 1 for all conditions, inferring instantaneous one-dimensional crystal growth followed by a decrease in hydrate nucleation and growth rates that could be attributed to the mass transfer resistance. Similar low exponent values were also reported by Susilo et al.[127], Luzi et al.[126], Silva et al.[154]. The corresponding AAD values are presented in Table 6. The model proposed by Lee et al.[132] was also used to analyze the kinetics of hydrate growth and the corresponding kinetic curves are presented in Figures S19, S20, S21, and S22, together with the regressed values in Table S2. As can be seen, Lee et al.[132] model predicted the initial kinetics of hydrate growth better than the JMAK model[125], nevertheless, later in time it reached a plateau and was unable to provide a close fit. This was also reflected in the AAD values (Table 6), where the maximum deviation in model prediction was determined at a later stage due to the presence of the adjustable parameter (α); suggesting the crystallization growth will eventually approach a constant. However, the real-time data demonstrated not only an exponential increase at first but also continuous growth with a reduced rate thereafter as the mass transfer (guest gas /H_2O) dominates crystallization in the porous medium. Conclusively, the predictive power of both JMAK[125] and Lee et al.[132] models revealed limitations in evaluating the hydrate growth at both the reaction-controlled and the diffusion-controlled regimes, resulting in a large deviation from the real-time data either at the beginning or later stages of the growth kinetics.

Given the limitations of single-step kinetic models, it is preferable to have an integrated multistep model to obtain a more accurate representation of the hydrate kinetics. Consequently, the model proposed by Hay[136] has been adapted in this work for evaluating the hydrate growth kinetics at both the reaction-controlled (primary growth stage) and the diffusion-controlled regimes (secondary growth stage). A more detailed version of Hay's model is presented in their earlier work on crystallization kinetics[136, 139, 155]. As can be seen from

454 (Eq. 10), the total water-to-hydrate conversion α_{WtH} can be classified into water-to-hydrate
455 conversion in the primary and secondary growth stage as shown in (Eq. 13)

$$\alpha_{WtH} = \alpha_{WtH,P} + \alpha_{WtH,S} \quad \text{(Eq. 13)}$$

456 The primary growth stage, which is attributed to the nucleation and rapid hydrate growth was
457 analyzed using the JMAK model[125] (Eq. 14), assuming that it ends before the onset of the
458 secondary growth stage (α_P), i.e. the diffusion-controlled regime.

$$\alpha_{WtH,P} = \alpha_P(1 - \exp(-k_p t^n)) \quad \text{(Eq. 14)}$$

459 The k_p and n are the same as described in (Eq. 10), and applying double logarithm, (Eq. 14)
460 can be rewritten as presented in (Eq. 15)

$$\ln(-\ln(1 - \alpha_{WtH,P}/\alpha_P)) = nln(t) + ln(k_P) \quad \text{(Eq. 15)}$$

461 In this analysis, α_P was used as an adjustable parameter and its value was chosen from the best
462 linear fit of the data to (Eq. 15) as determined by R^2 (for Ring-PMO at 276 K: Figure 12 and
463 the corresponding value of $ln(k_p)$ was determined from the intercept (Figures S23 and S24).
464 In every case, the exponent n value was set to 1 assuming one-dimensional growth. The water-
465 to-hydrate conversion in the second stage is defined as shown in (Eq. 16)

$$\alpha_{WtH,S} = \alpha_{WtH,P}(k_s t^{0.5}) \quad \text{(Eq. 16)}$$

466 Substituting (Eq. 16) and (Eq. 14) in (Eq. 13) results in the overall kinetic model as presented
467 in (Eq. 10). The kinetic rate constant for the secondary growth or crystallization stage was
468 obtained from the slope of the linear fit by plotting $\left[\left(\frac{\alpha_{WtH}-\alpha_P}{\alpha_P}\right)\right]$ vs $t^{0.5}$ (Figures S25 and S26).
469 The corresponding rate constants k_P, k_s and α_P for all the experiments performed in this work
470 are presented in Table 5. As shown in Table 5, the secondary kinetic rate constant (k_s), curtails
471 to a lower value after the first stage of growth in both SBA-15 C8 and Ring-PMO irrespective
472 of the driving force applied and this can be attributed to slower conversion rates due to mass
473 transfer resistance in these porous mediums upon achieving certain water-to-hydrate

conversion. As already mentioned above, the multistage kinetic model showed better predictions in the hydrate kinetics (Figures 13, 14, S27, S28) compared to the predictions from the JMAK[125] and Lee et al.[132] models, which is further highlighted in AAD values (Table 6). The contribution of primary and secondary-stage hydrate growth on water-to-hydrate conversion can also be extracted from this multistage model; for instance, the secondary stage contributes about 23% to the overall water-to-hydrate conversion for 200% pore-volume saturated Ring-PMO at 276 K as shown in Figure 15.

Subsequently, the model with the lowest AAD from the real-time data was used to determine the apparent activation energy of CH_4 hydrate formation using the Arrhenius equation (Eq. 17) for the pore-volume saturations with the maximum CH_4 storage capacity.

$$k = A * \exp\left(-\frac{E_a}{RT}\right) \quad \text{(Eq. 17)}$$

A is the frequency factor (min^{-1}), E_a is the activation energy ($J.mol^{-1}$), T is the temperature in (K), R is the gas constant (8.314 $J.K^{-1}.mol^{-1}$) and k is the rate constant, which corresponds to k_p from (Eq. 10). The least-squares linear fit for 130% pore-volume saturation in SBA-15 C8 and 200% pore-volume saturation in Ring-PMO gave apparent activation energy, E_a of -79 $kJ.mol^{-1}$ and -124 $kJ.mol^{-1}$, respectively as shown in Figure 16. One of the frequently observed characteristics of hydrate formation is its large negative activation energy, which was also previously reported for the sI CH_4 hydrates[19, 156], sII propane hydrates[157], Di and trifluoromethane hydrates[158, 159], and sII THF-Argon hydrates[160]. Chen et al.[161] described this anti-Arrhenius behavior for CH_4 hydrates by hypothesizing that hydrate formation reaction (in the primary stage) proceeds faster at lower temperatures resulting in a higher yield of hydrate in a given time. However, no activation energy value was reported by them. An apparent activation energy value of -106 $kJ.mol^{-1}$ and -94 $kJ.mol^{-1}$ for CH_4 hydrates was reported by Vysniauskas and Bishnoi[19] and Kitamjima et al.[156], respectively. Most explanations on the crystallization kinetics exhibiting negative activation energy hypothesize

498 the competitive influence between crystal growth and nucleation[19, 162, 163]; however, the
499 most likely interpretation of this anti-Arrhenius trend or negative activation energy can be
500 linked to free energy change as a function of cluster size based on the theory of nucleation with
501 special properties of H_2O clathrates as explained by Barrer and Ruzicka[160], where the energy
502 barrier for enclathration decreases with decreasing temperature and simultaneously small
503 cluster sizes reaches criticality followed by an increased rate of nucleation. Furthermore,
504 hydrate formation being a physical reaction, the energies involved in reorganization/clustering
505 of H_2O molecules and interactions between H_2O-CH_4 are reported to be approximately between
506 (-47 kJ.mol^{-1} to -50 kJ.mol^{-1})[164-168] and (-17 to -19 kJ.mol^{-1})[169, 170] respectively, and
507 the maximum sum of ≈ -70 kJ.mol^{-1} supports the negative activation energies calculated in this
508 work. In addition, these negative apparent activation energy highlights the curve-fitting nature
509 of these models.
510
511 4.5. Characterization of SBA-15 C8/Ring-PMO post-hydrate formation
512 To evaluate the material's resilience towards hydrate growth, multiple characterization
513 methods were used to investigate any chemical or morphological alterations post-clathrate
514 formation. The FTIR spectra of SBA-15 C8 and Ring-PMO, presented in Figure 17, reveal no
515 significant differences from fresh materials (pre-clathrate condition), showing that no chemical
516 modification of the materials takes place. Similarly, the effect of the clathrate formation process
517 on the porosity of the materials was investigated by N_2 sorption, and the results are shown in
518 Figures 18(a) and 18(b). Upon careful analysis of the N_2 sorption isotherms of the SBA-15 C8
519 materials, only minor alterations in terms of surface areas (345 vs 325 m² g^{-1}) and total pore
520 volumes (0.49 vs 0.46 cm^3 g^{-1}) were observed upon being exposed to the clathrate formation
521 process. However, Ring-PMO has shown slightly more noticeable changes in the total pore
522 volume (0.99 vs 0.90 cm^3 g^{-1}) and BET surface area (849 vs 747 m² g^{-1}). In general, it can be

concluded that the materials lose fairly small but not substantial porosities upon clathrate formation, highlighting their viability as clathrate hydrate promoters for longer and multiple cycles. The XRD diffractograms of both the material's pre- and post-clathrate formation, as shown in Figure 19, clearly indicate the conservation of structural parameters upon being subjected to the clathrate formation conditions. Furthermore, the TEM images of SBA-15 C8 and Ring-PMO showed no morphological changes (Figure 20) post-clathrate formation. Close inspection of the images demonstrates the retention of the mesoporous channels within the materials, indicating the preservation of the porous structures throughout the clathrate formation process.

5. Conclusion

CH_4 hydrate formation and growth in the presence of mesoporous hydrophobic materials (SBA-15 C8 and Ring-PMO) was investigated at multiple pore-volume saturations and temperatures;(269 K, 274 K, and 276 K) with an experimental pressure of 6 MPa. The kinetic parameters, such as maximum gas uptake and water-to-hydrate conversion, were observed for both materials at the lowest temperature. A rapid hydrate growth was demonstrated by both materials, which is favorable for CH_4 storage applications. Nevertheless, SBA-15 C8 exhibited a relatively longer time than Ring-PMO to attain its maximum storage capacity irrespective of the driving force applied. An optimal pore-volume saturation of 130% for SBA-15 C8 and 200% for Ring-PMO was identified, beyond which a considerable depression in gas uptake was observed. At 269 K, a maximum storage capacity of 98.2 mmol CH_4/mol H_2O at 130% pore-volume saturation and 101.2 mmol CH_4/mol H_2O at 200% pore-volume saturation was determined for SBA-15 C8 and Ring-PMO, respectively. At these optimal pore-volume saturations, it was also found that the Ring-PMO material could store up to ≈ 3.2 times more CH_4 in the form of clathrate per gram of dry solid, compared to the SBA-15 C8 material.

548 Furthermore, the Ring-PMO displayed a total storage capacity of 6.5 wt.%, a factor ≈ 2.0 times
549 higher compared to the SBA-15 C8 material. Three different models were used for kinetic
550 modeling of CH_4 hydrate formation and growth in both the materials under all driving forces
551 and pore-volume saturations. A multistage kinetic model performed significantly better in
552 predicting the experimental data (water-to-hydrate conversion), with a low average absolute
553 deviation (AAD). The apparent activation energy values for SBA-15 C8 and Ring-PMO were
554 extracted from the best-fit kinetic model at 130% and 200% pore-volume saturation,
555 respectively. Both materials demonstrated an inverse temperature dependence on the reaction
556 rates, owing to negative apparent activation energy (-79 $kJ.mol^{-1}$: SBA-15 C8, -124 $kJ.mol^{-1}$:
557 Ring-PMO) which are also comparable with the values reported in the literature. Finally, no
558 morphological change was observed for both materials after many cycles of hydrate formation,
559 confirming the preservation of structural integrity. The results from this study conclude that
560 the tailored hydrophobic porous materials; SBA-15 C8 and Ring-PMO are suitable for
561 promoting CH_4 hydrate growth and are capable of overcoming the slow kinetics of typical CH_4
562 formation, paving the way for efficient storage and transportation.

Acknowledgement

All authors acknowledge VLAIO for Moonshot funding (ARCLATH, n° HBC.2019.0110, ARCLATH2, n° HBC.2021.0254). PVDV acknowledges UGent for BOFBAS2020000401 for the funding of the XRD diffractometer.

Corresponding author*

NithinBharadwaj.Kummamuru@uantwerpen.be Tel: +32 48 95 73 921

ORCID

Nithin B. Kummamuru: 0000-0003-2989-3079

Geert Watson: 0000-0002-2324-4521

Radu-George Ciocarlan: 0000-0003-3834-8339

Sammy W. Verbruggen: 0000-0003-2372-9630

Pegie Cool: 0000-0002-6632-2243

Pascal Van Der Voort: 0000-0002-1248-479X

Patrice Perreault: 0000-0002-9392-2113

Supplementary data

The supplementary data to this article can be found online at:

584 **Table 1.** Chemicals description

Chemical name	Source
Acetone	ChemLab
Potassium chloride (KCl)	ChemLab
Hydrogen chloride ($HCl_{(aq,\ 37\%)}$)	ChemLab
Pluronic P-123	Merck Life Science
Tetraethyl orthosilicate (TEOS)	Sigma Aldrich
Toluene	Fisher Scientific
organosilane 1,1,3,3,5,5–hexaethoxy-1,3,5-trisilacyclohexane (HETSCH)	Gelest
trimethoxy(octyl)silane	Gelest

585

586

587 **Table 2.** Properties of materials used in this work

	SBA-15	SBA-15 C8	Ring-PMO
S_{BET} ($m^2\ g^{-1}$)	676	345	849
V_{tot} ($cm^3\ g^{-1}$)[a]	0.78	0.49	0.99
Pore size (nm)[b]	5.5	4.7	8.0

[a] Determined at a relative pressure of 0.95
[b] Determined using the BJH method on the desorption branch

588

Table 3. Summary of CH_4 hydrate formation at different experimental conditions in this study

Condition	*P* (MPa)	*T* (K)	SBA-15 C8		Ring-PMO	
			NG_t (mmol CH_4/mol H_2O)	*WtH* (%)	NG_t (mmol CH_4/mol H_2O)	*WtH* (%)
70% pore-volume sat.	6	269	55.0	31.6	25.2	14.5
100% pore-volume sat.	6	269	69.0	39.7	49.7	28.6
130% pore-volume sat.	6	269	98.2	56.5	69.1	39.7
200% pore-volume sat.	6	269	82.9	47.7	101.2	58.2
350% pore-volume sat.	6	269	-	-	86.7	49.8
70% pore-volume sat.	6	274	39.7	22.8	N/H	N/H
100% pore-volume sat.	6	274	55.6	32.0	29.5	17.0
130% pore-volume sat.	6	274	88.0	50.6	52.4	30.1
200% pore-volume sat.	6	274	81.8	47.0	85.9	49.4
350% pore-volume sat.	6	274	-	-	78.9	45.4
70% pore-volume sat.	6	276	N/H	N/H	N/H	N/H
100% pore-volume sat.	6	276	N/H	N/H	N/H	N/H
130% pore-volume sat.	6	276	73.5	42.4	N/H	N/H
200% pore-volume sat.	6	276	72.9	41.9	75.5	43.4
350% pore-volume sat.	6	276	-	-	67.4	38.7

N/H: no hydrates observed, '- ': no experiments performed

Table 4. Comparison of the hydrate storage capacity (q_{CH4}^{w}), dry weight storage capacity (q_{CH4}^{A}) and total storage capacity (q_{CH4}^{T}) of both the materials, as determined at 269 K and 6 MPa.

	q_{CH4}^{w}(wt. %)	q_{CH4}^{A}(wt. %)	q_{CH4}^{T}(wt. %)
SBA-15 C8	8.0	5.4	3.3
Ring-PMO	9.4	17.2	6.5
[a] Determined at pore volume saturation of 130% [b] Determined at pore volume saturation of 200%			

Table 5. Regressed values of rate constants (k_P, k_s), (α_P) for Hay model[136] analyzed in this work.

SBA-15 C8	T (K)	Hay[136]		
		α_p	k_p (min^{-1})	k_s (min^{-1})
70% pore-volume sat.	269	0.23	1.06E-01	2.56E-02
100% pore-volume sat.	269	0.27	1.67E-01	3.37E-02
130% pore-volume sat.	269	0.42	2.12E-01	2.03E-02
70% pore-volume sat.	274	0.09	1.08E-01	1.03E-01
100% pore-volume sat.	274	0.19	7.23E-02	3.56E-02
130% pore-volume sat.	274	0.35	9.41E-02	2.26E-02
130% pore-volume sat.	276	0.29	9.31E-02	3.10E-02
Ring-PMO	T (K)	Hay[136]		
		α_p	k_p (min^{-1})	k_s (min^{-1})
70% pore-volume sat.	269	0.1	1.23E-01	3.75E-02
100% pore-volume sat.	269	0.26	1.40E-01	9.72E-03
130% pore-volume sat.	269	0.36	1.29E-01	7.06E-03
200% pore-volume sat.	269	0.54	1.27E-01	3.70E-03
100% pore-volume sat.	274	0.14	6.57E-02	1.32E-02
130% pore-volume sat.	274	0.23	7.00E-02	1.71E-02
200% pore-volume sat.	274	0.43	6.82E-02	6.78E-03
200% pore-volume sat.	276	0.35	2.71E-02	1.04E-02

Table 6. The AAD values from JMAK[125], Lee et al.[132], and Hay[136] models in predicting water-to-hydrate conversion in all the systems studied in this work

SBA-15 C8	T (K)	JMAK[125]	Lee et al.[132]	Hay[136]
		AAD	AAD	AAD
70% pore-volume sat.	269	1.1	1.1	0.7
100% pore-volume sat.	269	1.2	1.6	0.5
130% pore-volume sat.	269	1.0	2.5	0.6
70% pore-volume sat.	274	0.5	0.7	0.7
100% pore-volume sat.	274	0.9	1.3	0.6
130% pore-volume sat.	274	1.1	2.2	0.9
130% pore-volume sat.	276	1.3	1.4	1.1
Ring-PMO	T (K)	JMAK[125]	Lee et al.[132]	Hay[136]
		AAD	AAD	AAD
70% pore-volume sat.	269	0.7	0.4	0.3
100% pore-volume sat.	269	2.2	0.3	0.4
130% pore-volume sat.	269	2.1	0.5	0.3
200% pore-volume sat.	269	1.9	0.8	0.2
100% pore-volume sat.	274	1.2	0.2	0.3
130% pore-volume sat.	274	1.5	0.7	0.3
200% pore-volume sat.	274	2.4	0.8	0.2
200% pore-volume sat.	276	2.6	1.1	0.6

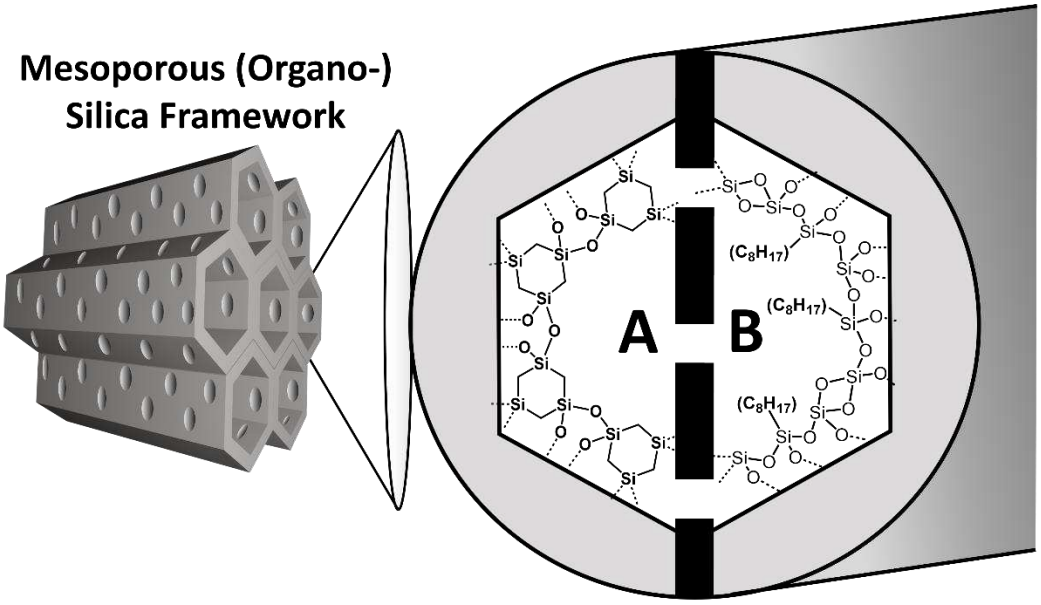

Figure 1. Chemical representation of both Ring-PMO (A) and SBA-15 C8 (B)

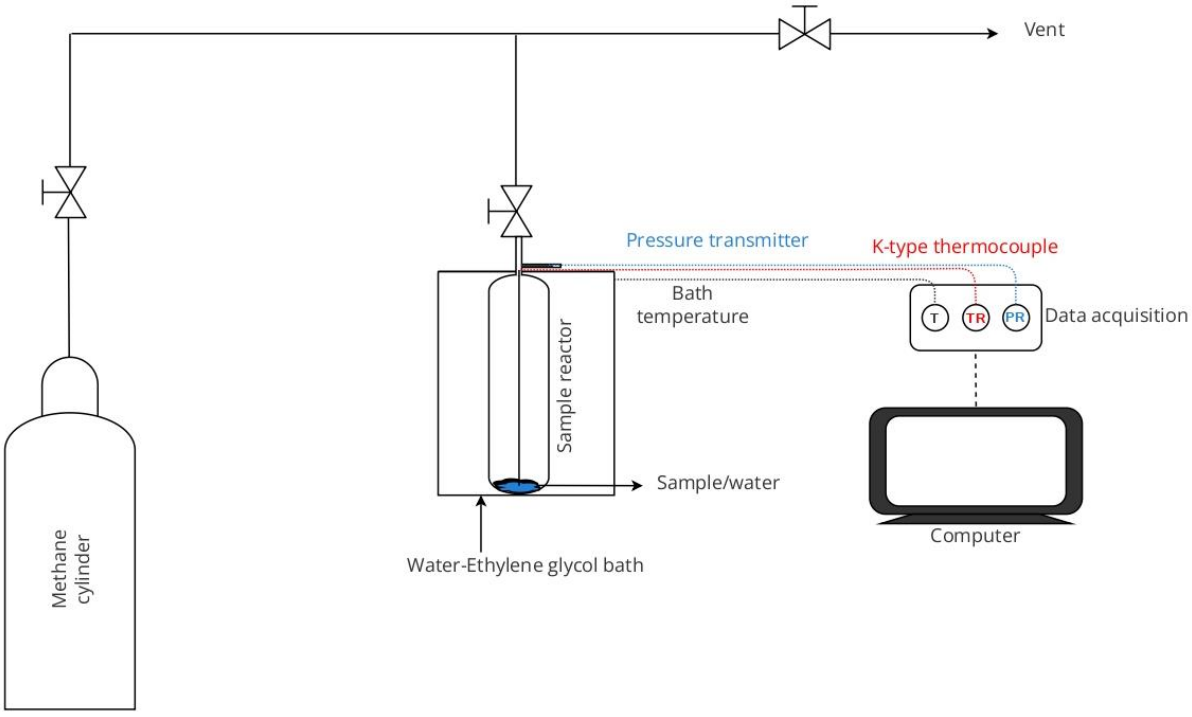

Figure 2. The schematic of the experimental setup for the study of CH_4 hydrate formation in SBA-15 C8 and Ring-PMO

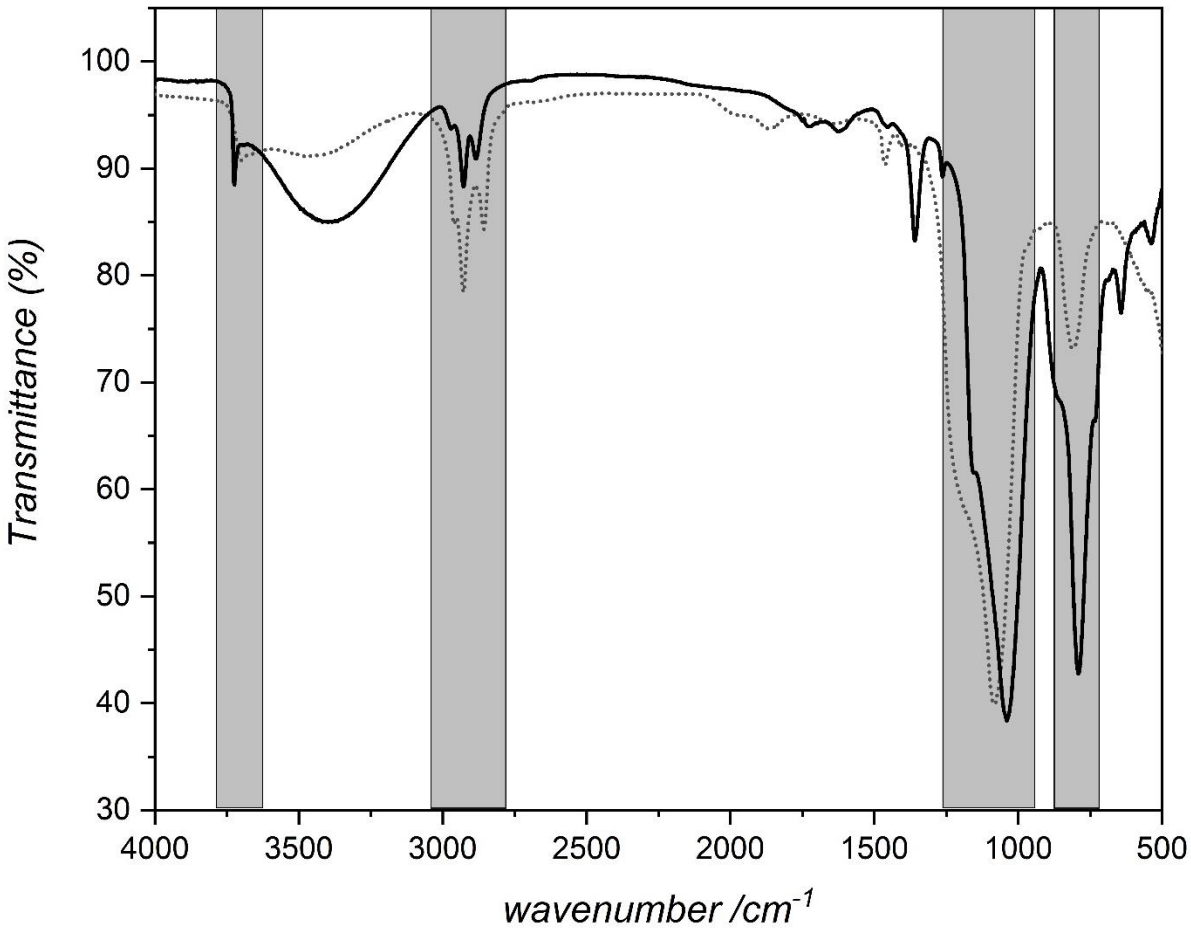

Figure 3. FT-IR recorded transmittance of both SBA-15 C8 (dotted line) and Ring-PMO (solid line) materials

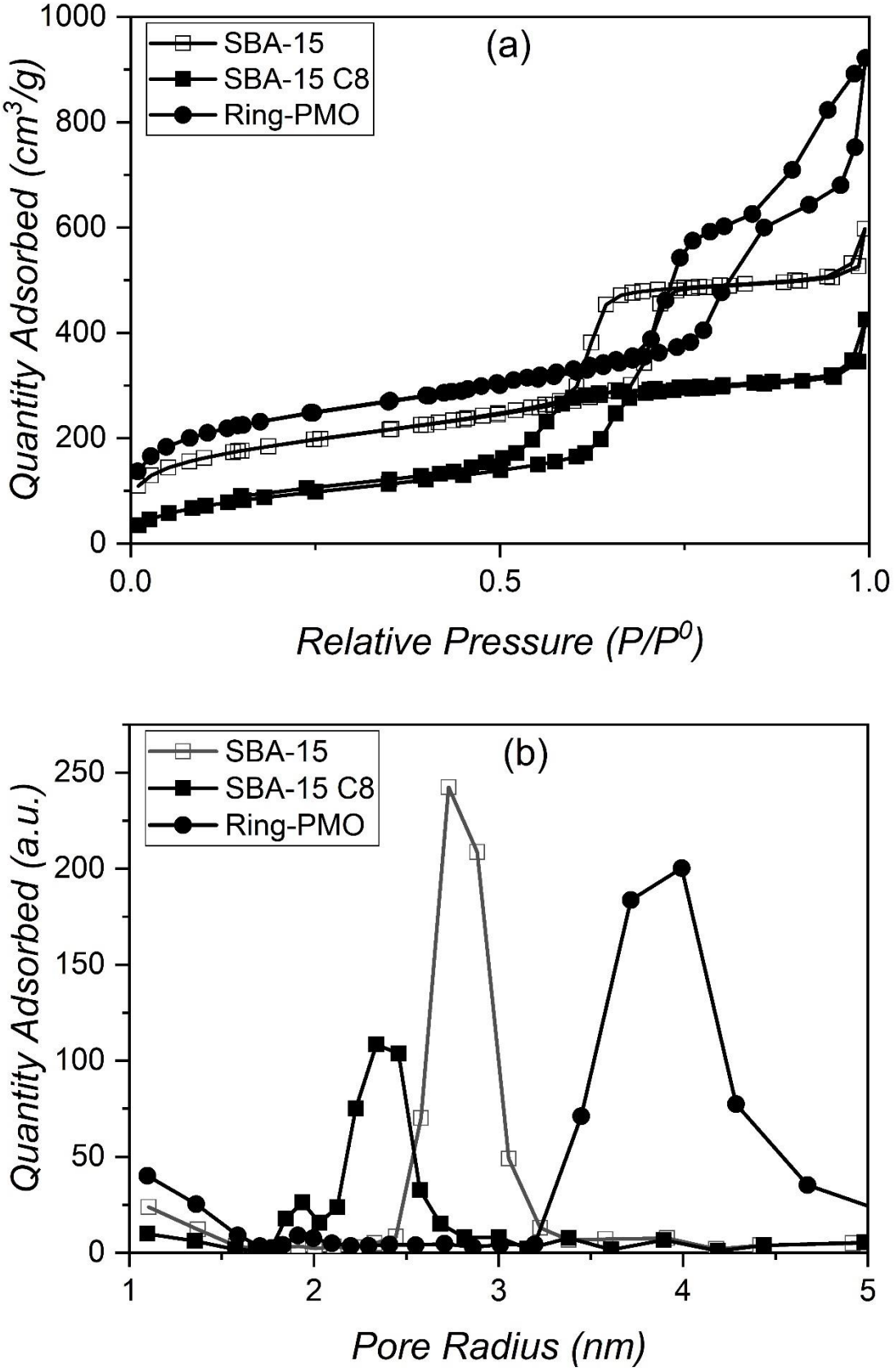

Figure 4. N_2 sorption isotherms (a) and corresponding pore sizes (b) of the SBA-15 materials pre- and post- alkyl modification together with N_2 isotherm of Ring-PMO

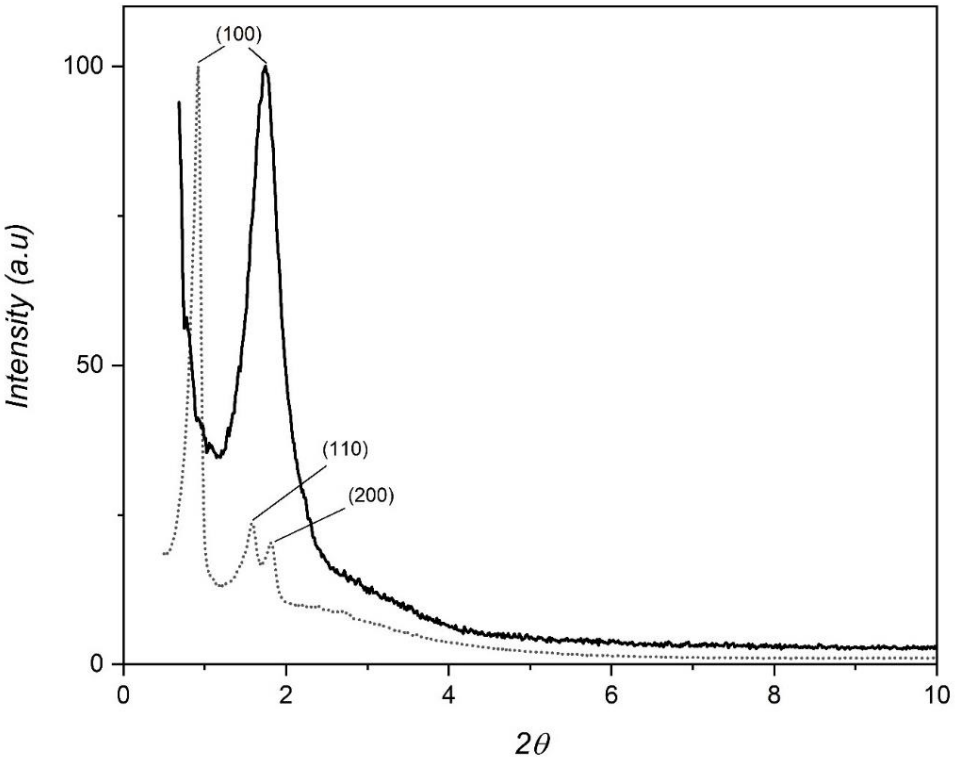

Figure 5. Overview of normalized XRD diffractograms of both SBA-15 C8 (dotted line) and Ring-PMO (solid line) materials

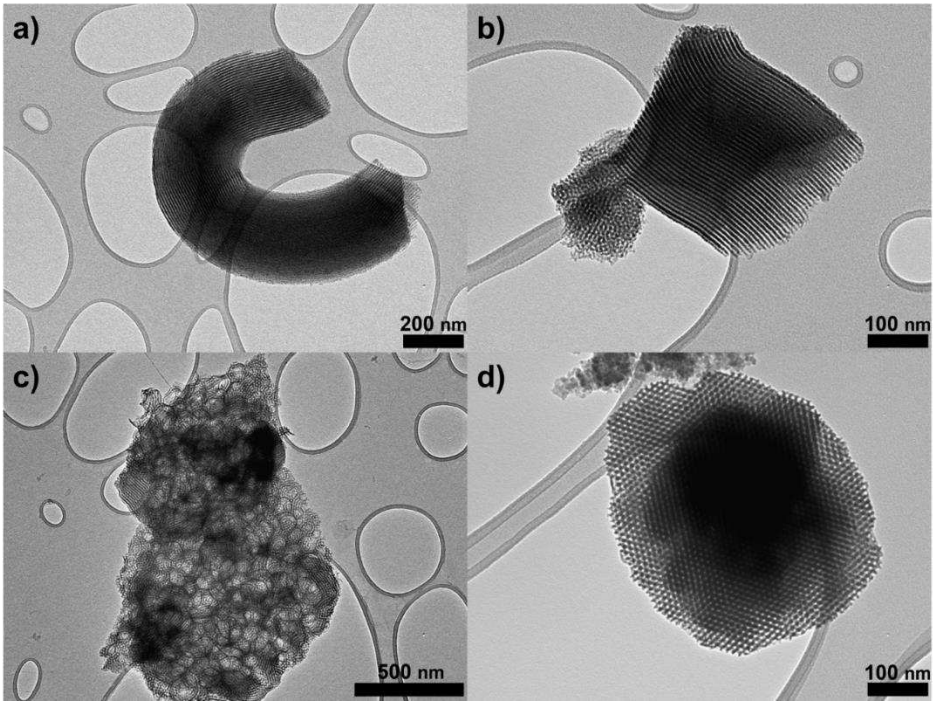

Figure 6. TEM images of the as-synthesized SBA-15 C8 (a and b) and Ring-PMO (c and d) materials

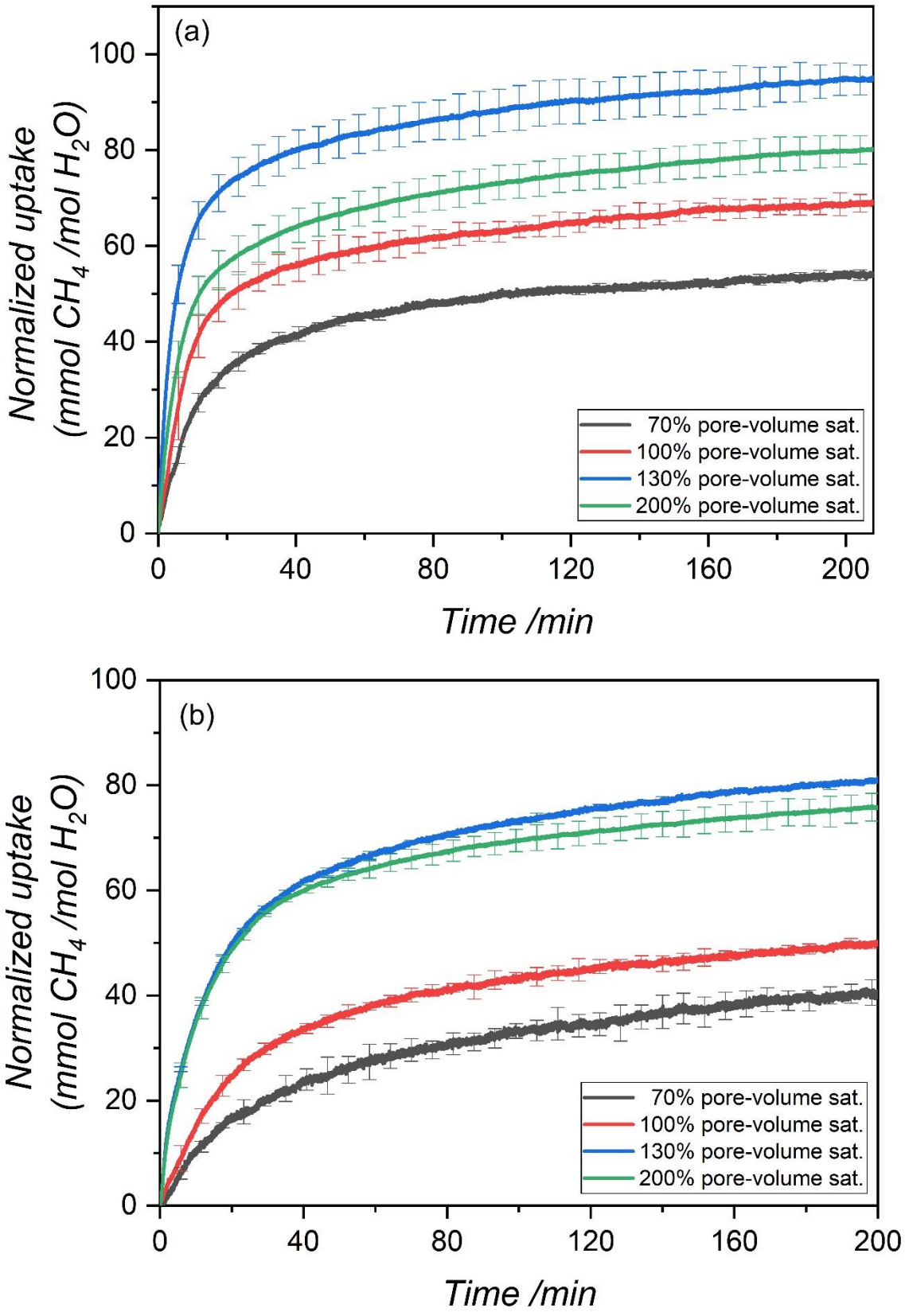

Figure 7. Normalized CH_4 uptake profiles during hydrate formation experiments conducted at 269 K (a) and 274 K (b) in SBA-15 C8 at multiple pore-volume saturations. Time zero corresponds to the nucleation point

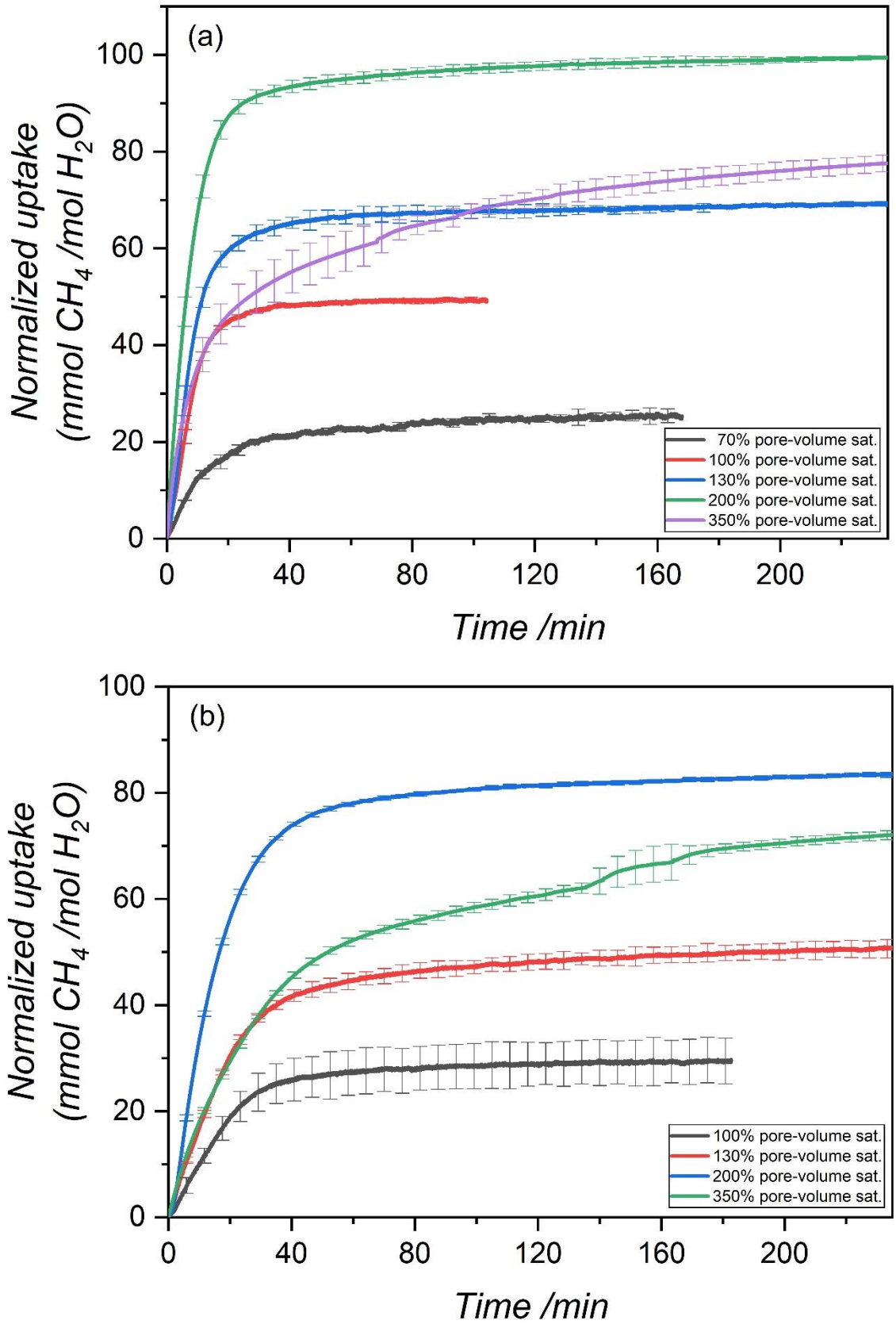

Figure 8. Normalized CH_4 uptake profiles during hydrate formation experiments conducted at 269 K (a) and 274 K (b) in Ring-PMO at multiple pore-volume saturations. Time zero corresponds to the nucleation point

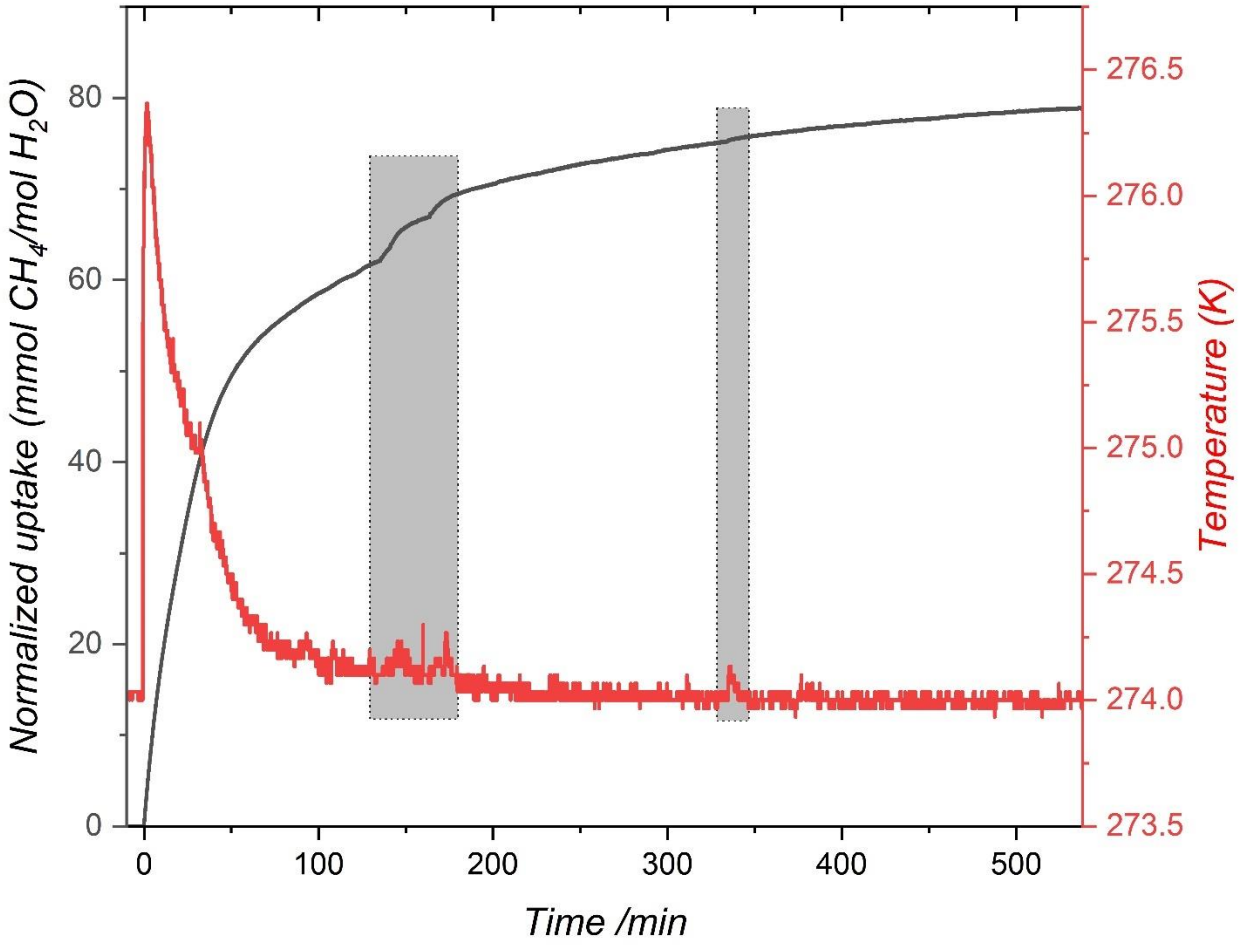

Figure 9. Multiple temperature spikes observed in Ring-PMO during CH_4 hydrate formation when saturated to 350% of pore-volume at 274 K

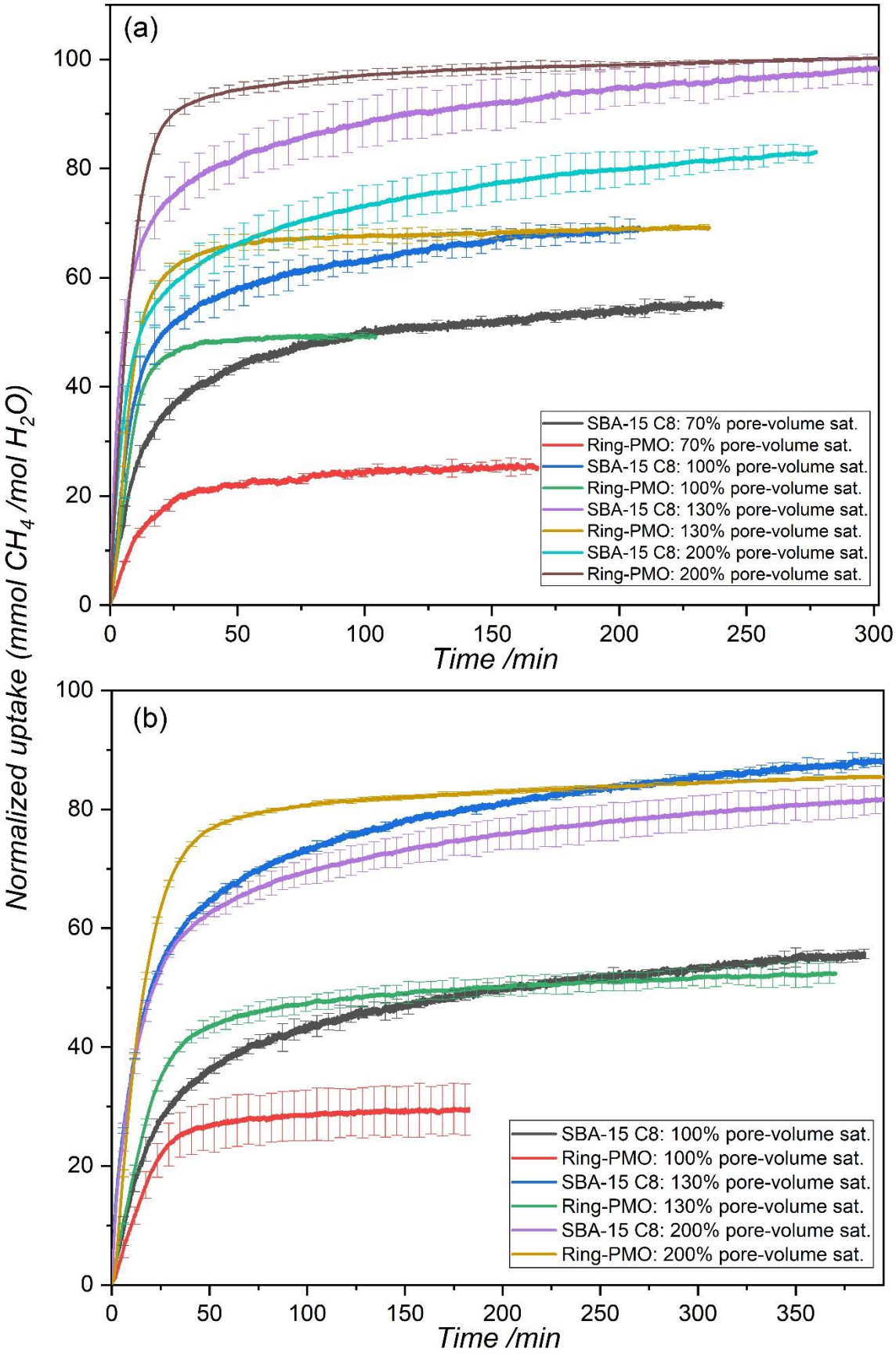

Figure 10. Comparison of CH_4 uptake behavior in SBA-15 C8 and Ring-PMO at 269 K (a) and 274 K (b) at multiple pore-volume saturations

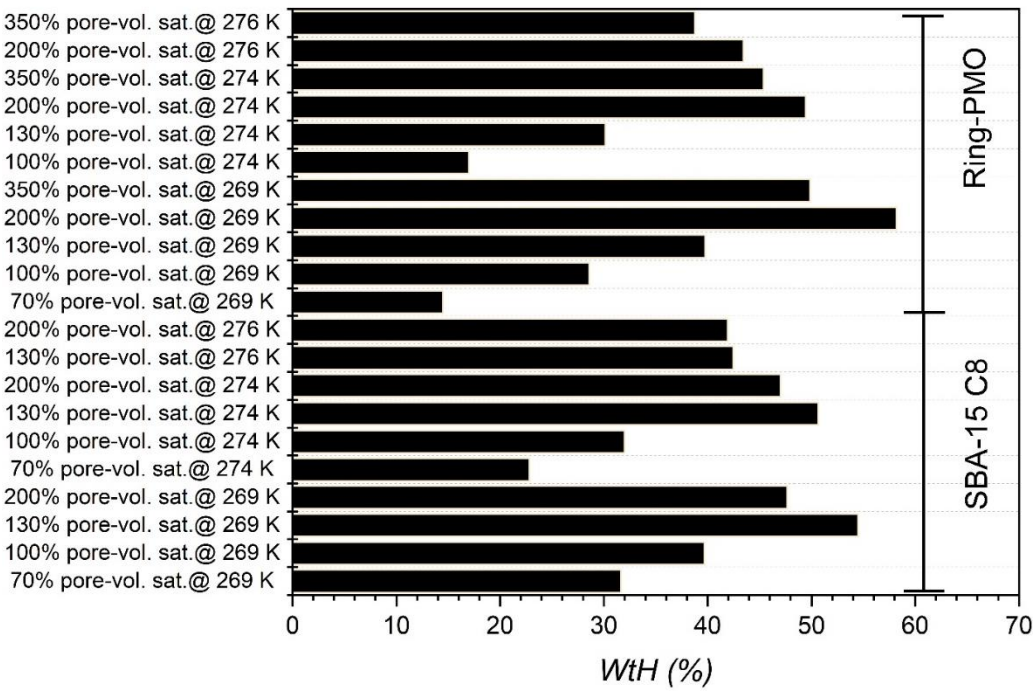

Figure 11. Water-to-hydrate conversion (%) in SBA-15 C8 and Ring-PMO at multiple operating conditions

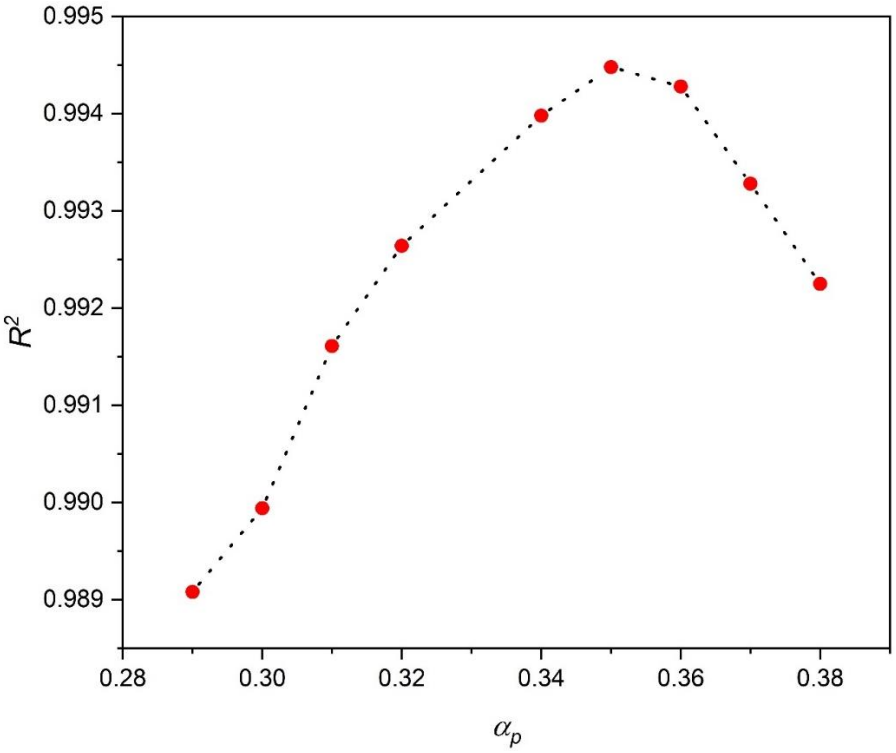

Figure 12. Effect of changing α_P on the degree of fit for 200% pore-volume saturation in Ring-PMO at 276 K

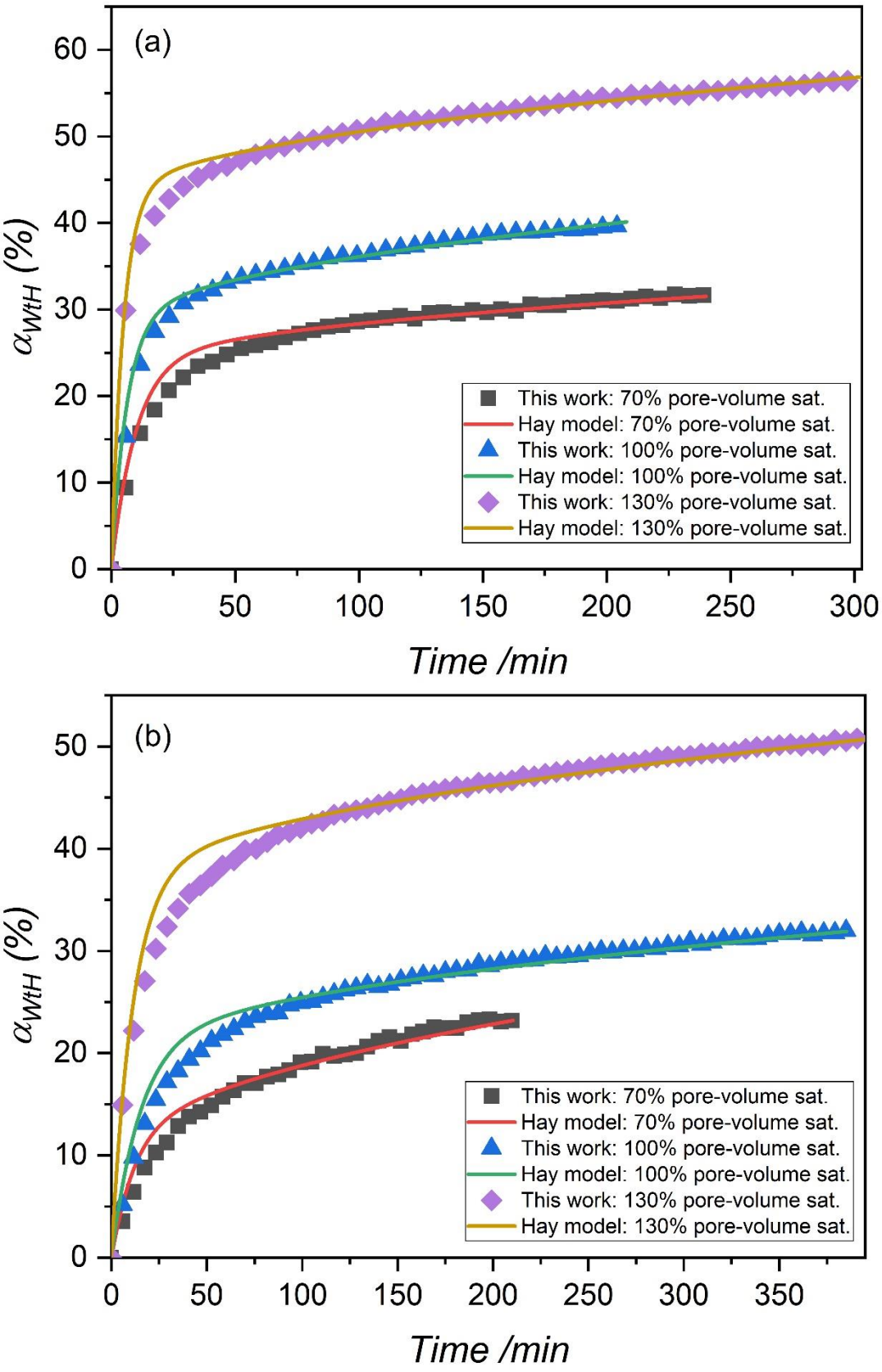

Figure 13. Comparing the Hay[136] model to experimental data for water-to-hydrate conversion (%) in SBA-15 C8 at 269 K (a) and 274 K (b)

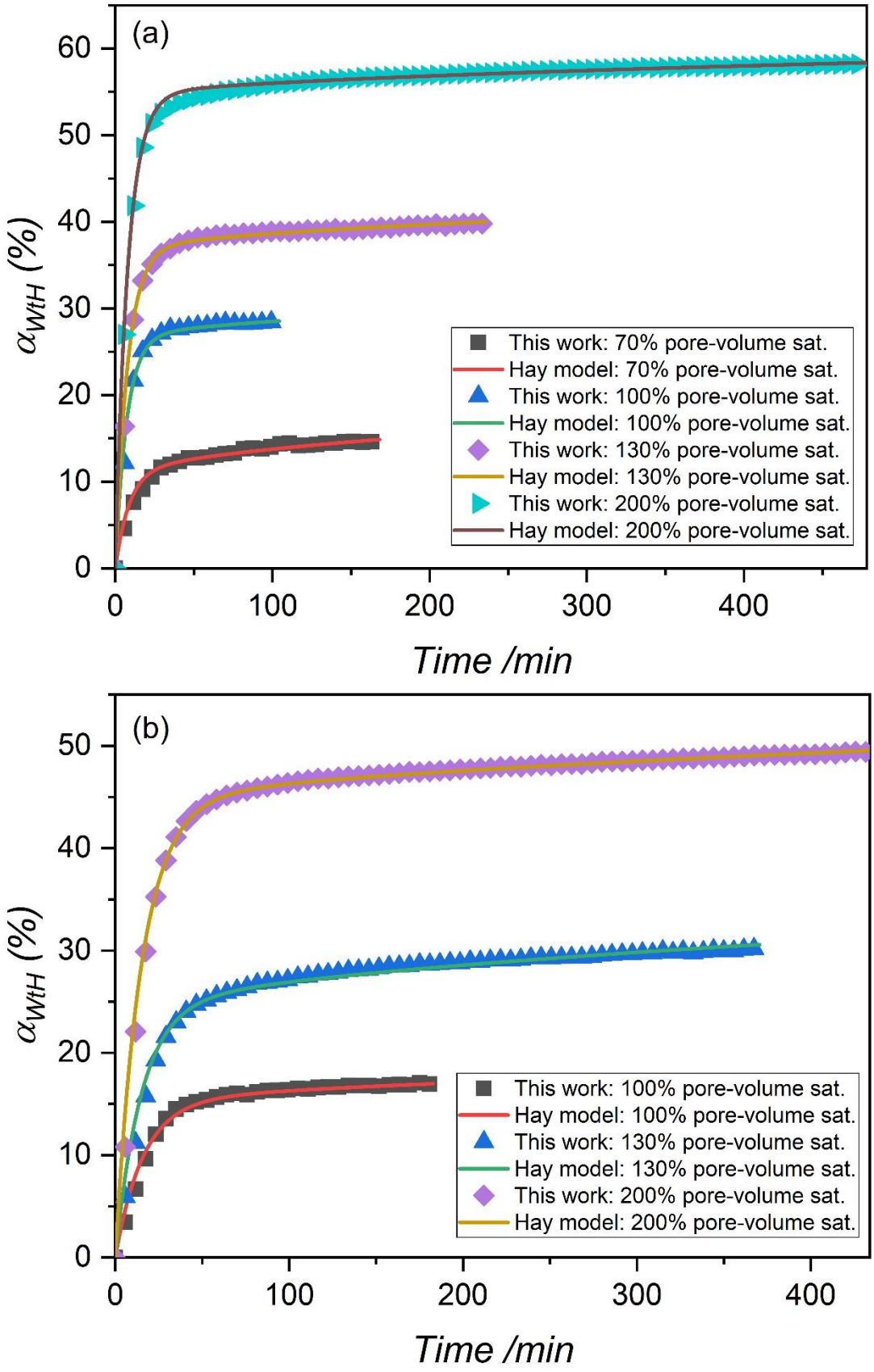

Figure 14. Comparing the Hay[136] model to experimental data for water-to-hydrate conversion (%) in Ring-PMO at 269 K (a) and 274 K (b)

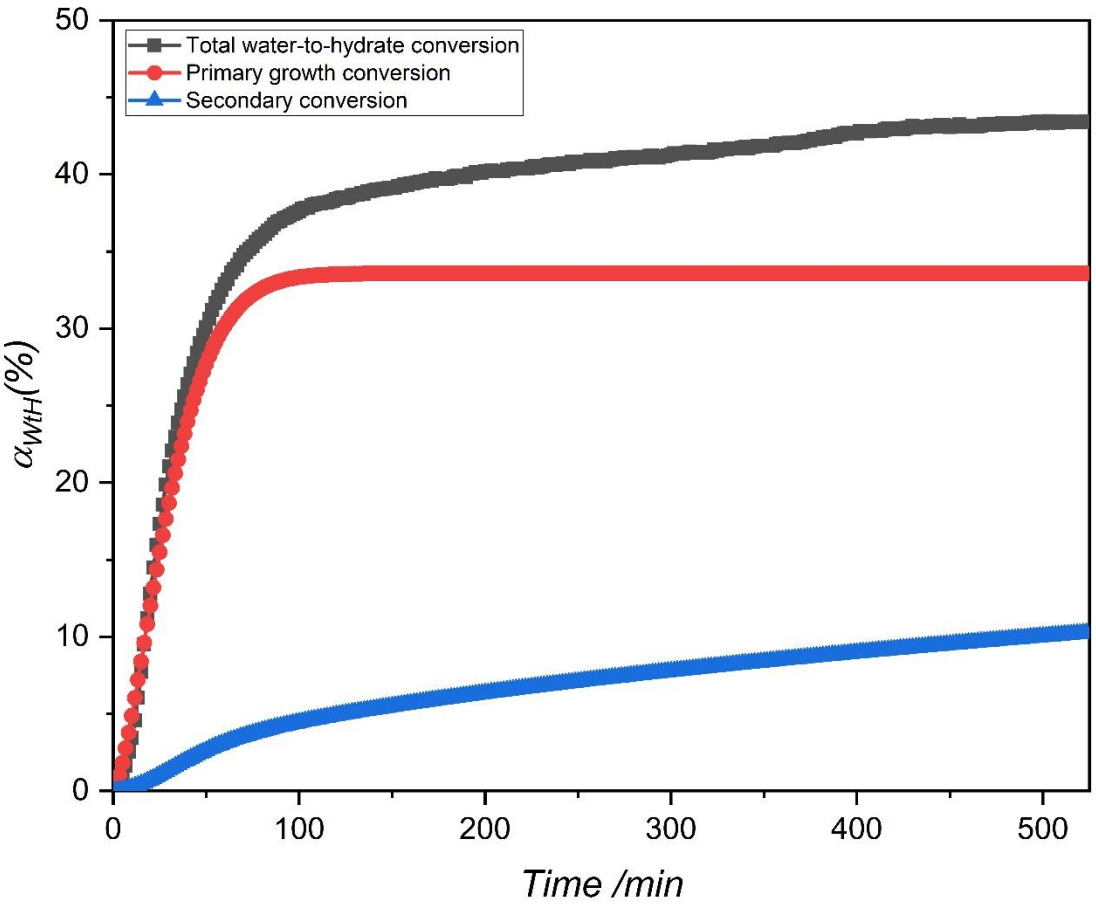

Figure 15. The contribution of primary and secondary-stage hydrate growth on water-to-hydrate conversion in 200% pore-volume saturated Ring-PMO at 276 K

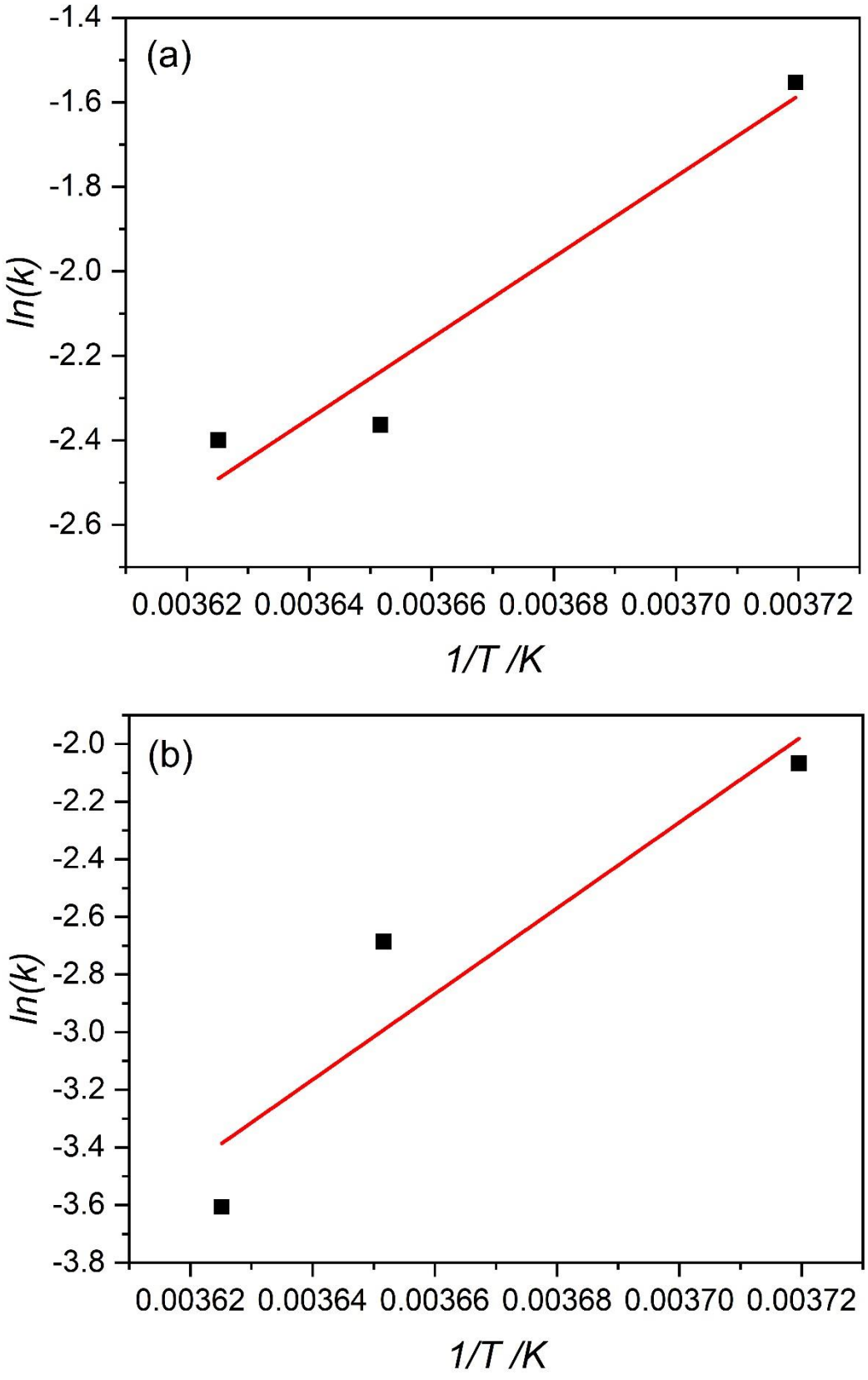

Figure 16. Arrhenius plots for (a) 130% pore-volume saturation: SBA-15 C8, (b) 200% pore-volume saturation: Ring-PMO

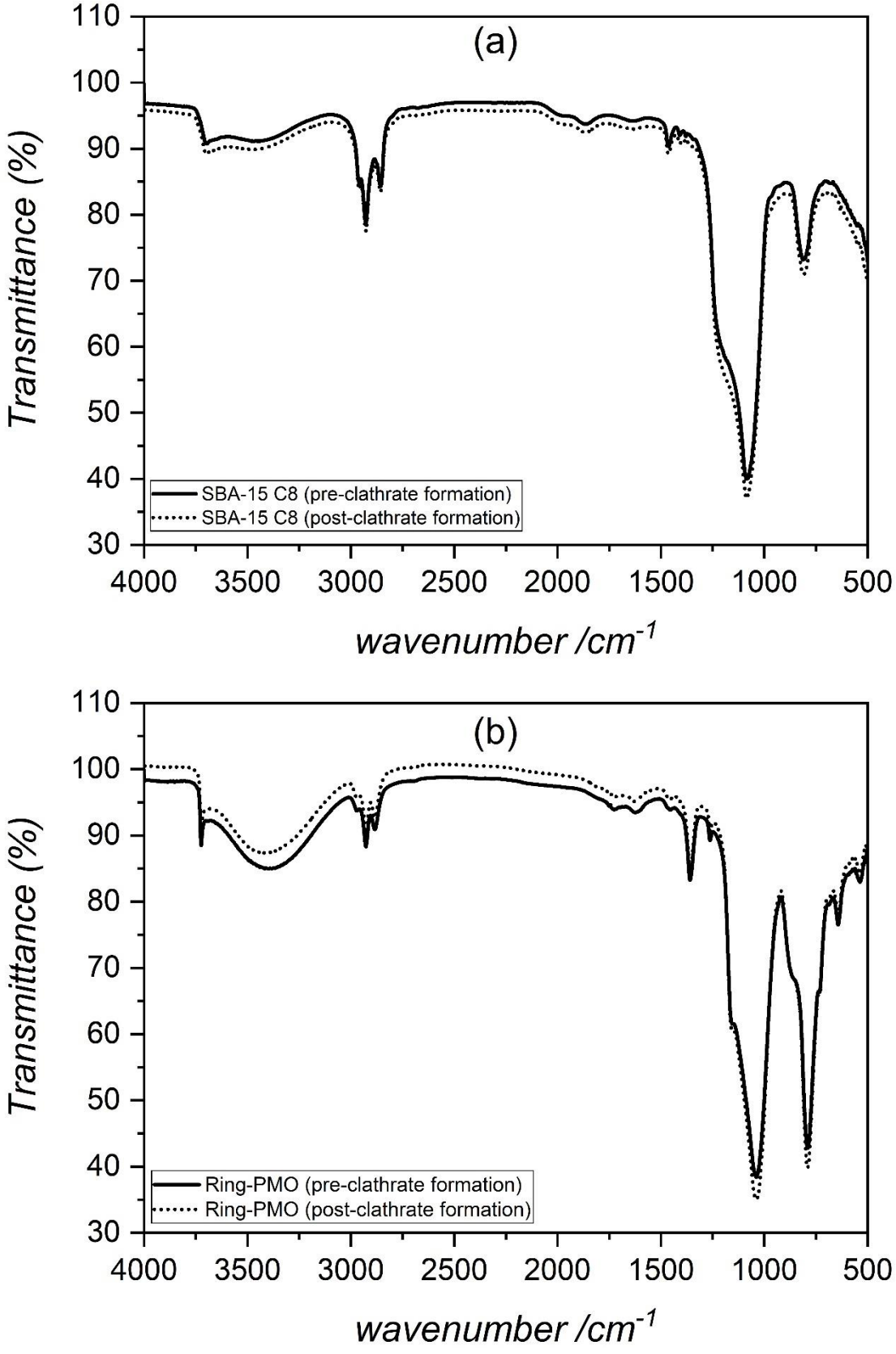

Figure 17. FT-IR recorded transmittance of both SBA-15 C8 (a) and Ring-PMO (b) materials pre- and post-clathrate formation

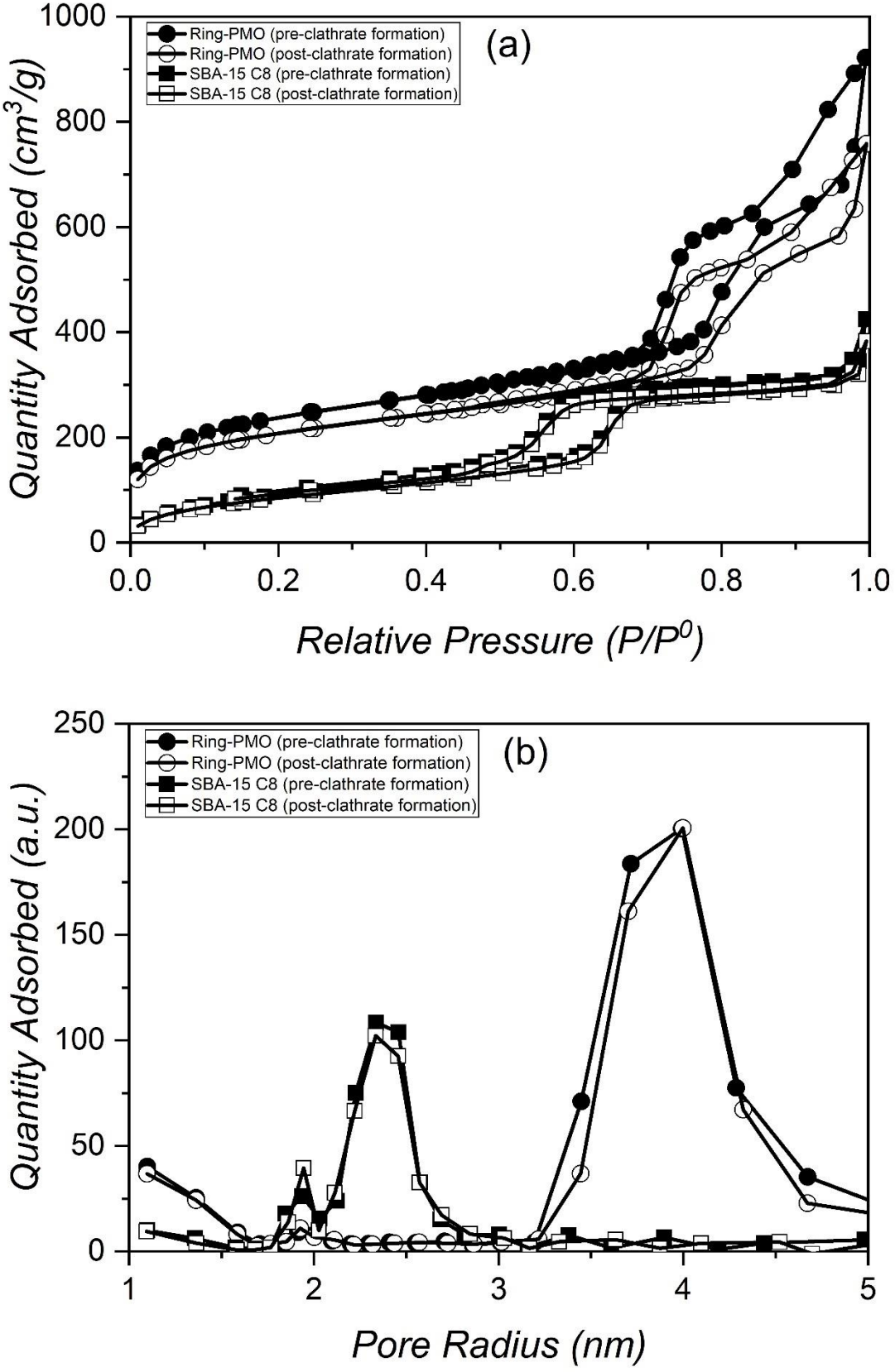

Figure 18. N_2 sorption isotherms (a) and corresponding pore sizes (b) of the SBA-15 C8 and Ring-PMO materials pre- and post-clathrate formation

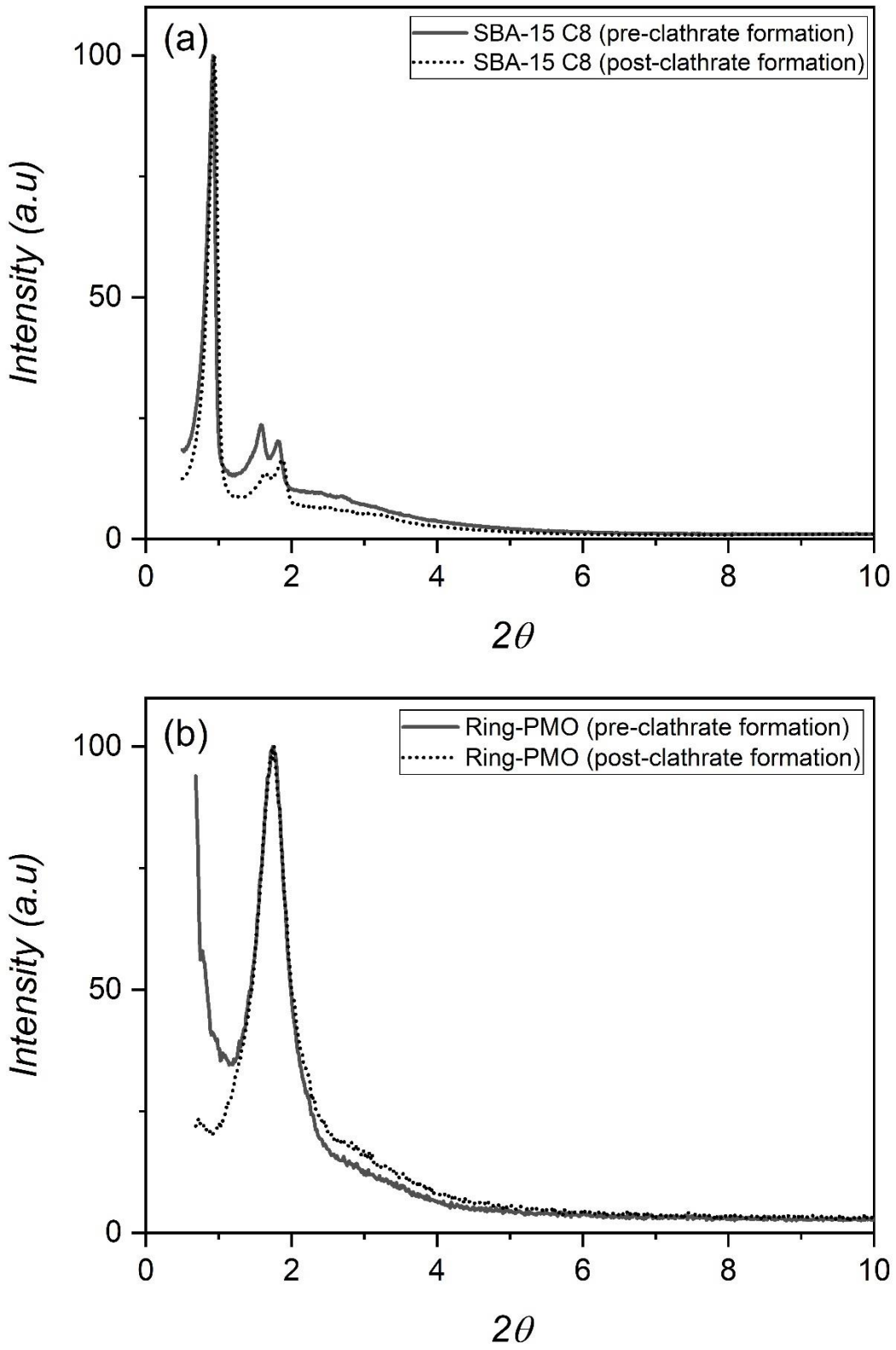

Figure 19. Overview of the normalized XRD diffractograms of both SBA-15 C8 (a) and Ring-PMO (b) materials pre- and post-clathrate formation, demonstrating the preservation of the structural parameters of both materials upon being exposed to clathrate formation

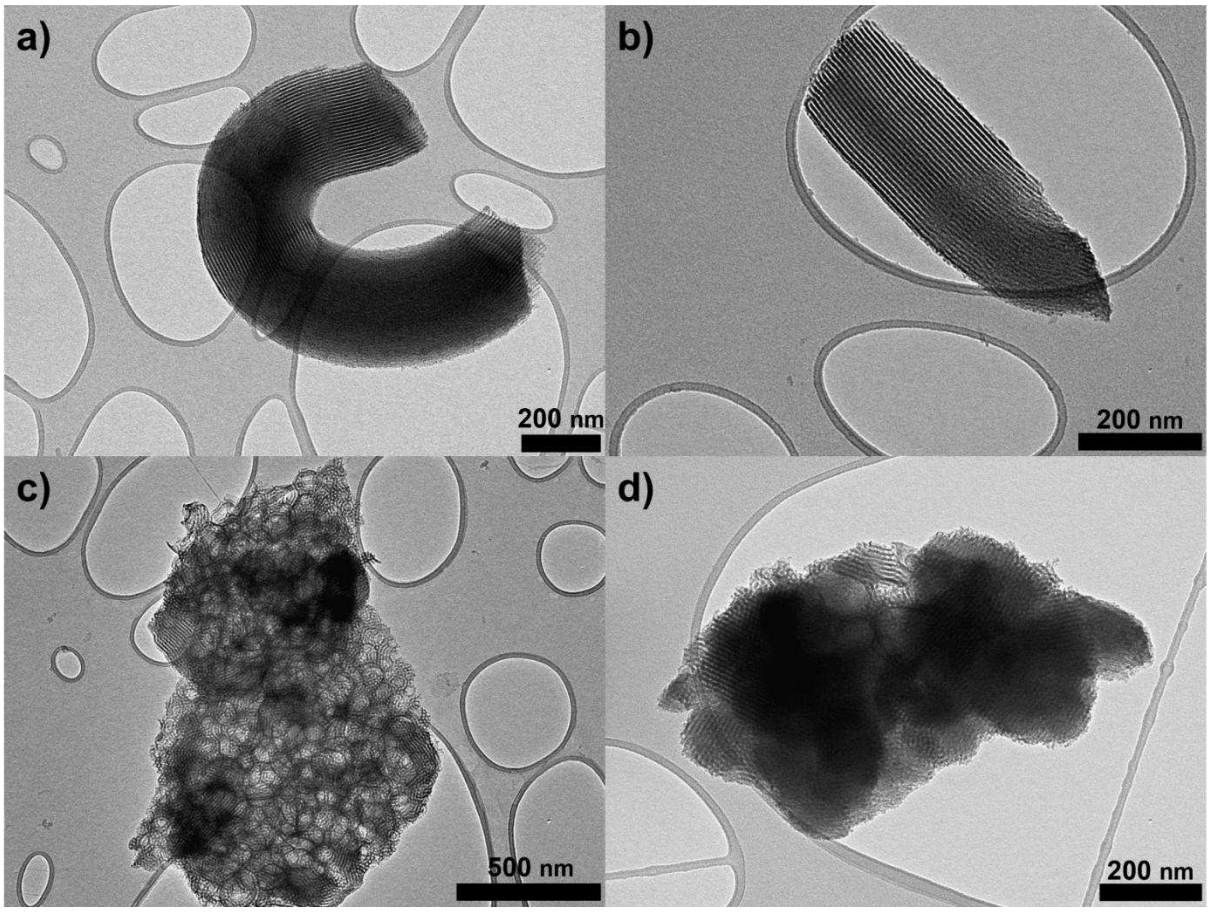

Figure 20. TEM images of pre-(fresh) and post-(used) clathrate formation in SBA-15 C8 (a and b respectively) and Ring-PMO (c and d respectively)

References

[1] IEA, World energy outlook 2021, Paris, 2021, https://www.iea.org/reports/world-energy-outlook-2021

[2] IEA, Global hydrogen review 2021, Paris, 2021, https://www.iea.org/reports/global-hydrogen-review-2021

[3] B. Viswanathan, Energy sources: Fundamentals of chemical conversion processes and applications, Elsevier, 2016.

[4] G. Bhattacharjee, M. N. Goh, S. E. K. Arumuganainar, Y. Zhang, P. Linga, Ultra-rapid uptake and the highly stable storage of methane as combustible ice, Energy Environ. Sci. 13 (2020) 4946-4961.

[5] A. Memetova, I. Tyagi, R. R. Karri, V. Kumar, K. Tyagi, Suhas, N. Memetov, A. Zelenin, T. Pasko, A. Gerasimova, D. Tarov, M. H. Dehghani, K. Singh, Porous carbon-based material as a sustainable alternative for the storage of natural gas (methane) and biogas (biomethane): A review, Chem. Eng. J. 446 (2022) 137373.

[6] D-z. Li, L. Chen, G. Liu, Z-y. Yuan, B-f. Li, X. Zhang, J-q. Wei, Porous metal–organic frameworks for methane storage and capture: status and challenges, New Carbon Mater. 36 (2021) 468-496.

[7] L. Ali, E. Mahmoud, Recent advances in the design of metal–organic frameworks for methane storage and delivery, J. Porous Mater. 28 (2021) 213-230.

[8] Dr. M. M. Deegan, M. R. Dworzak, A. J. Gosselin, K. J. Korman, Prof. Dr. Eric D. Bloch, Gas storage in porous molecular materials, Eur. J. Chem. 27 (2020) 4531-4547.

[9] E. Michaelis, R. Nie, D. Austin, Y. Yue, High surface area biocarbon monoliths for methane storage, GEE (2022).

[10] T. A. Makal, J. R. Li, W. Lu, H. C. Zhou, Methane storage in advanced porous materials, Chem. Soc. Rev. 41 (2012) 7761-7779.

[11] Y. F. Makogon, S. A. Holditch, T. Y. Makogon, Natural gas-hydrates — a potential energy source for the 21st century, J. Pet. Sci. Eng. 56 (2007) 14-31.

[12] S. Y. Lee, G. D. Holder, Methane hydrates potential as a future energy source, Fuel Process. Technol. 71 (2001) 181-186.

[13] A. Hassanpouryouzband, E. Joonaki, M. V. Farahani, S. Takeya, C. Ruppel, J. Yang, N. J. English, J. M. Schicks, K. Edlmann, H. Mehrabian, Z. M. Aman, B. Tohidi, Gas hydrates in sustainable chemistry, Chem. Soc. Rev. 49 (2020) 5225-5309.

[14] E. D. Sloan, C. A. Koh, Clathrate hydrates of natural gases, CRC Press, 2007.

[15] X. Lang, S. Fan, Y. Wang, Intensification of methane and hydrogen storage in clathrate hydrate and future prospect, J. Nat. Gas Chem. 19 (2010) 203-209.

[16] Z. M. Aman, C. A. Koh, Interfacial phenomena in gas hydrate systems, Chem. Soc. Rev. 45 (2016) 1678-1690.

[17] J. M. Lee, S. J. Cho, J. D. Lee, P. Linga, K. C. Kang, J. Lee, Insights into the kinetics of methane hydrate formation in a stirred tank reactor by In Situ raman spectroscopy, Energy Technol. 3 (2015) 925-934.

[18] W. F. Hao, J. Q. Wang, S. S. Fan, W. B. Hao, Study on methane hydration process in a semi-continuous stirred tank reactor, Energy Convers. Manage. 48 (2007) 954-960.

[19] A. Vysniauskas, P.R. Bishnoi, A kinetic study of methane hydrate formation, Chem. Eng. Sci. 38 (1983) 1061-1072.

[20] J. W. Du, H. J. Li, L. G. Wang, Cooperative effect of surfactant addition and gas-inducing agitation on methane hydrate formation rate, Fuel 230 (2018) 134-137.

[21] N. J. Kim, J. H. Lee, Y. S. Cho, W. Chun, Formation enhancement of methane hydrate for natural gas transport and storage, Energy 35 (2010) 2717-2722.

[22] H. Mimachi, M. Takahashi, S. Takeya, Y. Gotoh, A. Yoneyama, K. Hyodo, T. Takeda, T. Murayama, Effect of long-term storage and thermal history on the gas content of natural gas hydrate pellets under ambient pressure, Energy Fuels 29 (2015) 4827-4834.
[23] F. Rossi, M. Filipponi, B. Castellani, Investigation on a novel reactor for gas hydrate production, Appl. Energy 99 (2012) 167-172.
[24] K. Fukumoto, J. Tobe, R. Ohmura, Y. H. Mori, Hydrate formation using water spraying in a hydrophobic gas: a preliminary study, AlChE J. 47 (2001) 1899-1904.
[25] S. Fujita, K. Watanabe, Y. H. Mori, Clathrate-hydrate formation by water spraying onto a porous metal plate exuding a hydrophobic liquid coolant, AlChE J. 55 (2009) 1056-1064.
[26] H. Tsuji, R. Ohmura, Y. H. Mori, Forming structure-H hydrates using water spraying in methane gas: effects of chemical species of large-molecule guest substances, Energy Fuels 18 (2004) 418-424.
[27] Y. T. Luo, J. H. Zhu, S. S. Fan, G. J. Chen, Study on the kinetics of hydrate formation in a bubble column, Chem. Eng. Sci. 62 (2007) 1000-1009.
[28] Q. N. Lv, X. S. Li, C. G. Xu, Z. Y. Chen, Experimental investigation of the formation of cyclopentane-methane hydrate in a novel and large-size bubble column reactor, Ind. Eng. Chem. Res. 51 (2012) 5967-5975.
[29] Y. Zhong, R. E. Rogers, Surfactant effects on gas hydrate formation, Chem. Eng. Sci. 55 (2000) 4175-4187.
[30] W. Lin, G. J. Chen, C. Y. Sun, X. Q. Guo, Z. K. Wu, M. Y. Liang, L. T. Chen, L. Y. Yang, Effect of surfactant on the formation and dissociation kinetic behavior of methane hydrate, Chem. Eng. Sci. 59 (2004) 4449-4455.
[31] J. S. Zhang, S. Lee, J. W. Lee, Kinetics of methane hydrate formation from SDS solution, Ind. Eng. Chem. Res. 46 (2007) 6353-6359.
[32] C. Dicharry, J. Diaz, J-P. Torré, M. Ricaurte, Influence of the carbon chain length of a sulfate-based surfactant on the formation of CO_2,CH_4 and CO_2–CH_4 gas hydrates, Chem. Eng. Sci. 152 (2016) 736-745.
[33] A. Kumar, H. P. Veluswamy, R. Kumar, P. Linga, Kinetic promotion of mixed methane-THF hydrate by additives: Opportune to energy storage, Energy procedia 158 (2019) 5287-5292.
[34] H. P. Veluswamy, S. Kumar, R. Kumar, P. Rangsunvigit, P. Linga, Enhanced clathrate hydrate formation kinetics at near ambient temperatures and moderate pressures: Application to natural gas storage, Fuel 182 (2016) 907-919.
[35] H. P. Veluswamy, A. J. H. Wong, P. Babu, R. Kumar, S. Kulprathipanja, P. Rangsunvigit, P. Linga, Rapid methane hydrate formation to develop a cost effective large scale energy storage system, Chem. Eng. J. 290 (2016) 161-173.
[36] N. B. Kummamuru, P. Perreault, S. Lenaerts, A new generalized empirical correlation for predicting methane hydrate equilibrium conditions in pure water, Ind. Eng. Chem. Res. 60 (2021) 3474-3483.
[37] Q. Nasir, H. Suleman, Y. A. Elsheikh, A review on the role and impact of various additives as promoters/ inhibitors for gas hydrate formation, Int. J. Greenh. Gas Control. 76 (2020) 103211.
[38] Z. Wang, J. Duan, S. Chen, Y. Fu, X. Li, D. Wang, M. Zhang, Z. Zhang, D. Liu, F. Wang, A review on high-density methane storage in confined nanospace by adsorption-hydration hybrid technology, J. Energy Storage 50 (2022) 104195.
[39] L. Borchardt, M. E. Casco, J. Silvestre-Albero, Methane hydrate in confined spaces: An alternative storage system, ChemPhysChem 19 (2018) 1298-1314.
[40] J. Silvestre-Albero, Clathrate-Mediated gas storage in nanoporous materials, Nanoporous materials for gas storage, Springer, Singapore, 2019.

[41] D. H. Smith, J. W. Wilder, K. Seshadri, Methane hydrate equilibria in silica gels with broad pore-size distributions, AIChE J. 48 (2002) 393-400.
[42] Z. R. Chong, M. Yang, B. C. Khoo, P. Linga, Size effect of porous media on methane hydrate formation and dissociation in an excess gas environment, Ind. Eng. Chem. Res. 55 (2016) 7981-7991.
[43] P. Linga, C. Haligva, S. C. Nam, J. A. Ripmeester, P. Englezos, Gas hydrate formation in a variable volume bed of silica sand particles, Energy Fuels 23 (2009) 5496-5507.
[44] F. Filarsky, C. Schmuck, H. J. Schultz, Impact of modified silica beads on methane hydrate formation in a fixed-bed reactor, Ind. Eng. Chem. Res. 58 (2019) 16687-16695.
[45] Y. P. Handa, D. Y. Stupin, Thermodynamic properties and dissociation characteristics of methane and propane hydrates in 70-.ANG.-radius silica gel pores, J. Phys. Chem. 96 (1992) 8599-8603.
[46] Y. Seo, H. Lee, T. Uchida, Methane and carbon dioxide hydrate phase behavior in small porous silica gels: three-phase equilibrium determination and thermodynamic modeling, Langmuir 18 (2002) 9164-9170.
[47] V. C. Nair, S. Ramesh, G. A. Ramadass, J. S. Sangwai, Influence of thermal stimulation on the methane hydrate dissociation in porous media under confined reservoir, J. Pet. Sci. Eng. 147 (2016) 547-559.
[48] B. O. Carter, W. X. Wang, D. J. Adams, A. I. Cooper, Gas storage in ″dry water″ and ″dry gel″ clathrates, Langmuir 26 (2010) 3186-3193.
[49] W. X. Wang, C. L. Bray, D. J. Adams, A. I. Cooper, Methane storage in dry water gas hydrates, J. Am. Chem. Soc. 130 (2008) 11608-11609.
[50] J. L. Wang, R. J. Wang, R. H. Yoon, Y. Seol, Use of hydrophobic particles as kinetic promoters for gas hydrate formation, J. Chem. Eng. Data 60 (2015) 383-388.
[51] T. Park, J. Y. Lee, T. H. Kwon, Effect of pore size distribution on dissociation temperature depression and phase boundary shift of gas hydrate in various fine-grained sediments, Energy Fuels 32 (2018) 5321-5330.
[52] B. B. Ge, D. L. Zhong, Y. Y. Lu, Influence of water saturation and particle size on methane hydrate formation and dissociation in a fixed bed of silica sand, Energy procedia 157 (2019) 5402-5407.
[53] R. Wang, T. Liu, F. Ning, W. Ou, L. Zhang, Z. Wang, L. Peng, J. Sun, Z. Liu, T. Li, H. Sun, G. Jiang, Effect of hydrophilic silica nanoparticles on hydrate formation: Insight from the experimental study, J. Energy Chem. 30 (2019) 90-100.
[54] J. Liu, D. Liang, Investigation on methane hydrate formation in silica gel particles below the freezing point, RSC Adv. 9 (2019) 15022.
[55] J. Zhao, Y. Zhao, W. Liang, S. Song, Q. Gao, Semi-clathrate hydrate process of methane in porous media-mesoporous materials of SBA-15, Fuel 220 (2018) 446-452.
[56] S. P. Kang, Y. Seo, W. Jang, Kinetics of methane and carbon dioxide hydrate formation in silica gel pores, Energy Fuels 23 (2009) 3711-3715.
[57] S. P. Kang, W. J. Lee, Formation characteristics of synthesized natural gas hydrates in meso and macroporous silica gels, J. Phys. Chem. B 114 (2010) 6973-3978.
[58] S. A. Bagherzadeh, I. L. Moudrakovski, J. A. Ripmeester, P. Englezos, Magnetic resonance imaging of gas hydrate formation in a bed of silica sand particles, Energy Fuels 25 (2011) 3083-3092.
[59] M. E. Casco, S. Grätz, D. Wallacher, N. Grimm, D. M. Többens, M. Bilo, N. Speil, M. Fröba, L. Borchardt, Influence of surface wettability on methane hydrate formation in hydrophilic and hydrophobic mesoporous silicas, Chem. Eng. J. 405 (2021) 126955.
[60] S. Takeya, H. Fujihisa, Y. Gotoh, V. Istomin, E. Chuvilin, H. Sakagami, A. Hachikubo, Methane clathrate hydrates formed within hydrophilic and hydrophobic media:

Kinetics of dissociation and distortion of host structure, J. Phys. Chem. C 117 (2013) 7081-7085.
[61] M. E. Casco, E. Zhang, S. Grätz, S. Krause, V. Bon, D. Wallacher, N. Grimm, D. M. Többens, T. Hauß, L. Borchardt, Experimental evidence of confined methane hydrate in hydrophilic and hydrophobic model carbons, J. Phys. Chem. C 123 (2019) 24071-24079.
[62] M. E. Casco, J. S. Albero, A. J. Ramírez-Cuesta, F. Rey, J. L. Jordá, A. Bansode, A. Urakawa, I. Peral, M. M. Escandell, K. Kaneko, F. R. Reinoso, Methane hydrate formation in confined nanospace can surpass nature, Nat. Commun. 6 (2015) 6432.
[63] S. S. Park, S. B. Lee, N. J. Kim, Effect of multi-walled carbon nanotubes on methane hydrate formation, J. Ind. Eng. Chem. 16 (2010) 551-555.
[64] C.C. Collados, J. F. Pérez, M. M. Escandell, A. Missyul, J. S. Albero, Effect of additives in the nucleation and growth of methane hydrates confined in a high-surface area activated carbon material, Chem. Eng. J. 388 (2020) 124224.
[65] A. Siangsai, P. Rangsunvigit, B. Kitiyanan, S. Kulprathipanja, P. Linga, Investigation on the roles of activated carbon particle sizes on methane hydrate formation and dissociation, Chem. Eng. Sci. 126 (2015) 383-389.
[66] L. Zhou, Y. Sun, Y. P. Zhou, Enhancement of the methane storage on activated carbon by pre-adsorbed water, AlChE J. 48 (2002) 2412-2416.
[67] A. Perrin, J.F.M. A. Celzard, G. Furdin, Improved methane storage capacities by sorption on wet active carbons, Carbon 42 (2004) 1249-1256.
[68] L. Zhou, J. Liu, W. Su, Y. Sun, Y. Zhou, Progress in studies of natural gas storage with wet adsorbents, Energy Fuels 24 (2010) 3789-3795.
[69] Y. Zhou, Y. Wang, H. Chen, L. Zhou, Methane storage in wet activated carbon: studies on the charging/discharging process, Carbon 43 (2005) 2007-2012.
[70] A. Celzard, J. F. Marêché, Optimal wetting of active carbons for methane hydrate formation, Fuel 85 (2006) 957-966.
[71] C. Cuadrado-Collados, F. Fauth, I. S. Basanez, M. M. Escandell, J. Silvestre-Albero, Methane hydrate formation in the confined nanospace of activated carbons in seawater environment, Micropor. Mesopor. Mat. 255 (2018) 220-225.
[72] G. Zhang, X. Shi, R. Zhang, K. Chao, F. Wang, Promotion of activated carbon on the nucleation and growth kinetics of methane hydrates, Front. Chem. 8 (2020) 934.
[73] C. Cuadrado-Collados, A. A. A. Majid, M. M. Escandell, L. L. Daemen, A. Missyul, C. Koh, J. Silvestre-Albero, Freezing/melting of water in the confined nanospace of carbon materials: Effect of an external stimulus, Carbon 158 (2020) 346-355.
[74] J. Liu, Y. Zhou, Y. Sun, W. Su, L. Zhou, Methane storage in wet carbon of tailored pore sizes, Carbon 49 (2011) 3731-3736.
[75] J. Pasieka, S. Coulombe, P. Servio, Investigating the effects of hydrophobic and hydrophilic multi-wall carbon nanotubes on methane hydrate growth kinetics, Chem. Eng. Sci. 104 (2013) 998-1002.
[76] M.S. G. Zhang, B. Liu, F. Wang, Adsorption-induced two-way nanoconvection enhances nucleation and growth kinetics of methane hydrates in confined porespace, Chem. Eng. J. 396 (2020) 125256.
[77] H. Liu, S. Zhan, P. Guo, S. Fan, S. Zhang, Understanding the characteristic of methane hydrate equilibrium in materials and its potential application, Chem. Eng. J. 349 (2018) 775-781.
[78] Z. He, K. Zhang, J. Jiang, Formation of CH_4 hydrate in a mesoporous metal-organic framework MIL-101: Mechanistic insights from microsecond molecular dynamics simulations, J. Phys. Chem. Lett. 10 (2019) 7002-7008.

[79] D. Kim, Y. H. Ahn, H. Lee, Phase equilibria of CO_2 and CH_4 hydrates in intergranular meso/macro pores of MIL-53 metal organic framework, J. Chem. Eng. Data 60 (2015) 2178-2185.
[80] S. Denning, A. A. Majid, J. M. Lucero, J. M. Crawford, M. A. Carreon, C. A. Koh, Metal–Organic Framework HKUST-1 promotes methane hydrate formation for improved gas storage capacity, ACS Appl. Mater. Interfaces 12 (2020) 53510-53518.
[81] C. Cuadrado-Collados, G. Mouchaham, L. Daemen, Y. Cheng, A. Ramirez-Cuesta, H. Aggarwal, A. Missyul, M. Eddaoudi, Y. Belmabkhout, J. Silvestre-Albero, Quest for an optimal methane hydrate formation in the pores of hydrolytically stable metal–organic frameworks, J. Am. Chem. Soc. 142 (2020) 13391-13397.
[82] L. Mu, B. Liu, H. Liu, Y. Yang, C. Sun, G. Chen, A novel method to improve the gas storage capacity of ZIF-8, J. Mater. Chem. 22 (2012) 12246-12252.
[83] M. E. Casco, F. Rey, J. L. Jordá, S. Rudić, F. Fauth, M. M. Escandell, F. R. Reinoso, E. V. Ramos-Fernández, J. S. Albero, Paving the way for methane hydrate formation on metal−organic frameworks (MOFs), Chem. Sci. 7 (2016) 3658-3666.
[84] S. Denning, A. A. A. Majid, J. M. Lucero, J. M. Crawford, M. A. Carreon, C. A. Koh, Methane hydrate growth promoted by microporous zeolitic imidazolate frameworks ZIF-8 and ZIF-67 for enhanced methane storage, ACS Sustainable Chem. Eng. 9 (2021) 9001-9010.
[85] Y. Zhao, J. Zhao, W. Liang, Q. Gao, D. Yang, Semi-clathrate hydrate process of methane in porous media-microporous materials of 5A-type zeolites, Fuel 220 (2018) 185-191.
[86] E. Andres-Garcia, A. Dikhtiarenko, F. Fauth, J. Silvestre-Albero, E. V. Ramos-Fernández, J. Gascon, C. Avelino, F. Kapteijn, Methane hydrates: nucleation in microporous materials, Chem. Eng. J. 360 (2019) 569-576.
[87] X. Zang, J. Du, D. Liang, S. Fan, C. Tang, Influence of A-type zeolite on methane hydrate formation, Chin. J. Chem. Eng. 17 (2009) 854-859.
[88] N.-J. Kim, S.-S. Park, S.-W. Shin, J.-H. Hyun, W. Chun, An experimental investigation into the effects of zeolites on the formation of methane hydrates, Int. J. Energy Res. 39 (2015) 26-32.
[89] T. Uchida, T. Ebinuma, T. Ishizaki, Dissociation condition measurements of methane hydrate in confined small pores of porous glass, J. Phys. Chem. B 103 (1999) 3659-3662.
[90] G. C. Fitzgerald, M. Castaldi, J. M. Schicks, Methane hydrate formation and thermal based dissociation behavior in silica glass bead porous media, Ind. Eng. Chem. Res. 53 (2014) 6840-6854.
[91] H. J. Li, L. G. Wang, Hydrophobized particles can accelerate nucleation of clathrate hydrates, Fuel 140 (2015) 440-445.
[92] N. N. Nguyen, A. V. Nguyen, K. M. Steel, L. X. Dang, M. Galib, Interfacial gas enrichment at hydrophobic surfaces and the origin of promotion of gas hydrate formation by hydrophobic solid particles., J. Phys. Chem. C 121 (2017) 3830-3840.
[93] N. B. Kummamuru, S. W. Verbruggen, S. Lenaerts, P. Perreault, Experimental investigation of methane hydrate formation in the presence of metallic packing, Fuel 323 (2022) 124269.
[94] Z. Deng, S. Fan, Y. Wang, X. Lang, G. Li, Enhance hydrates formation with stainless steel fiber for high capacity methane storage, Chin. J. Chem. Eng. (2022).
[95] P. Hu, D. Chen, M. Zi , G. Wu, Effects of carbon steel corrosion on the methane hydrate formation and dissociation, Fuel 230 (2018) 126-133.
[96] L. Yang, S. S. Fan, Y. H. Wang, X. M. Lang, D. L. Xie, Accelerated formation of methane hydrate in aluminum foam, Ind. Eng. Chem. Res. 50 (2011) 11563-11569.

[97] S. Fan, L. Yang, X. Lang, Y. Wang, D. Xie, Kinetics and thermal analysis of methane hydrate formation in aluminum foam, Chem. Eng. Sci. 82 (2012) 185-193.
[98] X. Liu, L. Tian, D. Chen, G. Wu, Accelerated formation of methane hydrates in the porous SiC foam ceramic packed reactor, Fuel 257 (2019) 115858.
[99] Y. Guo, W. Xiao, W. Pu, J. Hu, J. Zhao, L. Zhang, CH_4 nanobubbles on the hydrophobic solid−water interface serving as the nucleation sites of methane hydrate, Langmuir 34 (2018) 10181-10186.
[100] D. Guo, W. Ou, F. Ning, B. Fang, Y. Liang, S. U. Din, L. Zhang, Effects of hydrophilic and hydrophobic nano-$CaCO_3$ on kinetics of hydrate formation, Energy Sci. Eng. 10 (2022) 507-524.
[101] N. N. Nguyen, A. V. Nguyen, Hydrophobic effect on gas hydrate formation in the presence of additives, Energy Fuels 31 (2017) 10311-10323.
[102] Y. Li, M. Chen, H. Song, P. Yuan, D. Liu, B. Zhang, H. Bu, Methane hydrate formation in the stacking of kaolinite particles with different surface contacts as nanoreactors: A molecular dynamics simulation study, 186 (2020) 105439.
[103] Z. Wang, J. Duan, S. Chen, Y. Fu, Y. Zhang, D. Wang, J. Pei, D. Liu, Molecular insights into hybrid CH_4 physisorption-hydrate growth in hydrophobic metal–organic framework ZIF-8: Implications for CH_4 storage, Chem. Eng. J. 430 (2022) 132901.
[104] F. Filarsky, C. Schmuck, H. J. Schultz, Development of a surface-active coating for promoted gas hydrate formation, Chem. Ing. Tech. 91 (2019) 85-91.
[105] E. A. Müller, L. F. Rull, L. F. Vega, K. E. Gubbins, Adsorption of water on activated carbons: A molecular simulation study, J. Phys. Chem. 100 (1996) 1189-1196.
[106] C. L. McCallum, T. J. Bandosz, S. C. McGrother, E. A. Müller, K. E. Gubbins, A molecular model for adsorption of water on activated carbon: comparison of simulation and experiment, Langmuir 15 (1999) 533-544.
[107] T. Ohba, K. Kaneko, Surface oxygen-dependent water cluster growth in carbon nanospaces with GCMC simulation-aided in situ SAXS, J. Phys. Chem. C 111 (2007) 6207-6214.
[108] M. S. P. Sansom, P. C. Biggin, Water at the nanoscale, Nature 414 (2001).
[109] T. Ohba, H. Kanoh, K. Kaneko, Affinity transformation from hydrophilicity to hydrophobicity of water molecules on the basis of adsorption of water in graphitic nanopores, J. Am. Chem. Soc. 126 (2004) 1560-1562.
[110] T. Ohba, T. Omori, H. Kanoh, M. Yudasaka, S. Iijima, K. Kaneko, Interstitial nanopore change of single wall carbon nanohorn assemblies with high temperature treatment, Chem. Phys. Lett. 389 (2004) 332-336.
[111] Z. Li, R.-H.Yoon, Thermodynamics of hydrophobic interaction between silica surfaces coated with octadecyltrichlorosilane, J. Colloid Interface Sci. 392 (2013) 369-375.
[112] J. Miyawaki, T. Kanda, T. Suzuki, T. Okui, Y. Maeda, K. Kaneko, Macroscopic evidence of enhanced formation of methane nanohydrates in hydrophobic nanospaces, J. Phys. Chem. B 102 (1998) 2187-2192.
[113] N. N. Nguyen, M. Galib, A. V. Nguyen, Critical review on gas hydrate formation at solid surfaces and in confined spaces-Why and how does interfacial regime matter?, Energy Fuels 34 (2020) 6751-6760.
[114] T. Iiyama, K. Nishikawa, T. Otowa, K. Kaneko, An ordered water molecular assembly structure in a slit-shaped carbon nanospace, J. Phys. Chem. 99 (1995) 10075-10076.
[115] H. Li, P. Stanwix, Z. Aman, M. Johns, E. May, L. Wang, Raman spectroscopic studies of clathrate hydrate formation in the presence of hydrophobized particles, J. Phys. Chem. 120 (2016) 417-424.

[116] P. G. M. Mileo, S. M. J. Rogge, M. Houlleberghs, E. Breynaert, J. A. Martens, V. V. Speybroeck, Interfacial study of clathrates confined in reversed silica pores, J. Mater. Chem. A 9 (2021) 21835.
[117] S. Denning, A. A. A. Majid, C. A. Koh, Stability and growth of methane hydrates in confined media for carbon sequestration, J. Phys. Chem. C 126 (2022) 11800-11809.
[118] L. Borchardt, W. Nickel, M. Casco, I. Senkovska, V. Bon, D. Wallacher, N. Grimm, S. Krausea, J. Silvestre-Albero, Illuminating solid gas storage in confined spaces – methane hydrate formation in porous model carbons, Phys. Chem. Chem. Phys. 18 (2016) 20607.
[119] V. Meynen, P. Cool, E. F. Vansant, Verified syntheses of mesoporous materials, Microporous Mesoporous Mater. 125 (2009) 170-223.
[120] J. Zou, R. Rezaee, Effect of particle size on high-pressure methane adsorption of coal, Pet. Res. 1 (2016) 53-58.
[121] J. M. Smith, H. V. Ness, M. Abbott, M. Swihart, Introduction to chemical engineering thermodynamics, 8 ed., McGraw-Hill Education, 2015.
[122] P. S. R. Prasad, B. S. Kiran, K. Sowjanya, Enhanced methane gas storage in the form of hydrates: role of the confined water molecules in silica powders, RSC Adv. 10 (2020) 17795-17804.
[123] M. Avrami, Kinetics of phase change. i general theory, J. Chem. Phys. 7 (1939) 1103.
[124] M. Avrami, Kinetics of phase change. ii transformation-time relations for random distribution of nuclei, J. Chem. Phys. 8 (1940) 212.
[125] M. Fanfoni, M. Tomellini, The Johnson-Mehl-Avrami-Kohnogorov model: A brief review, Nouv Cim D 20 (1998) 1171-1182.
[126] M. Luzi, J. M. Schicks, R. Naumann, J. Erzinger, Systematic kinetic studies on mixed gas hydrates by Raman spectroscopy and powder X-ray diffraction, J. Chem. Thermodynamics 48 (2012) 28-35.
[127] R. Susilo, J. A. Ripmeester, P. Englezos, Methane conversion rate into structure H hydrate crystals from Ic, AIChE J. 53 (2007) 2451-2460.
[128] I. L. Moudrakovski, A. A. Sanchez, C. I. Ratcliffe, J. A. Ripmeester, Nucleation and growth of hydrates on ice surfaces: new insights from 129xe nmr experiments with hyperpolarized xenon, J. Phys. Chem. B 105 (2001) 12338-12347.
[129] A. Nambiar, P. Babu, P. Linga, CO_2 capture using the clathrate hydrate process employing cellulose foam as a porous media, Can. J. Chem. 93 (2015) 1-7.
[130] J. Zhao, L. Zhang, X. Chen, Y. Zhang, Y. Liu, Y. Song, Combined replacement and depressurization methane hydrate recovery method, Energy Explor. Exploit. 34 (2016) 129-139.
[131] A. Kumar, D. Khatri, J. Dong, R. Kumar, Crystallization kinetics for carbon dioxide gas hydrate in fixed bed and stirred tank reactor, Korean J. Chem. Eng. 33 (2016) 1922-1930.
[132] J-w. Lee, M-K. Chun, K-M. Lee, Y-J. Kim, H. Lee, Phase equilibria and kinetic behavior of CO_2 hydrate in electrolyte and porous media solutions: application to ocean sequestration of CO_2, Korean J. Chem. Eng. 19 (2002) 673-678.
[133] C. E. Holley Jr, W. J. Worlton, R. K. Zeigler, Compressibility factors and fugacity coefficients calculated from the beattie-bridgeman equation of state for hydrogen, nitrogen, oxygen, carbon dioxide, ammonia, methane, and helium, United States, 1958,
[134] H. Liang, D. Guan, K. Shi, L. Yang, L. Zhang, J. Zhao, Y. Song, Characterizing mass-transfer mechanism during gas hydrate formation from water droplets, Chem. Eng. J. 428 (2022) 132626.

[135] J. Zhao, H. Liang, L. Yang, X. Zhang, Y. Song, A. K. Sum, Growth kinetics and gas diffusion in formation of gas hydrates from ice, J. Phys. Chem. C 124 (2020) 12999-13007.
[136] J. N. Hay, Secondary crystallization kinetics, Polymer Crystallization 1 (2018) e10007.
[137] Z. Chen, J. N. Hay, M. J. Jenkins, The effect of secondary crystallization on crystallization kinetics – Polyethylene terephthalate revisited, Eur. Polym. J. 81 (2016) 216-223.
[138] C. Zhang, G. Liu, Y. Zhao, K. Wang, X. Dong, Z. Li, L. Wang, D. Wang, Exploring the polymorphic behavior of aβ-nucleatedpropylene-ethylene random copolymer under shear flow, Polymer Crystallization 3 (2020) e10105.
[139] K. Phillipson, M. J. Jenkins, J. N. Hay, The effect of a secondary process on crystallization kinetics – Poly (ϵ-caprolactone) revisited, Eur. Polym. J. 84 (2016) 708-714.
[140] E. D. Sloan, CSMHYD, 1998.
[141] J. Zhou, W. Su, Y. Sun, S. Deng, X. Wang, Enhanced CO_2 sorption on ordered mesoporous carbon CMK-3 in the presence of water, J. Chem. Eng. Data 61 (2016) 1348-1352.
[142] P. Linga, C. Haligva, S. C. Nam , J. A. Ripmeester, P. Englezos, Recovery of methane from hydrate formed in a variable volume bed of silica sand particles, Energy Fuels 23 (2009) 5508-5516.
[143] P. Mekala, P. Babu, J. S. Sangwai, P. Linga, Formation and dissociation kinetics of methane hydrates in seawater and silica sand, Energy Fuels 28 (2014) 2708-2716.
[144] T. J. Kneafsey, L. Tomutsa, G. J. Moridis, Y. Seol, B. M. Freifeld, C. E. Taylor, A. Gupta, Methane hydrate formation and dissociation in a partially saturated core-scale sand sample, J. Pet. Sci. Eng. 56 (2007) 108-126.
[145] P. Mekala, M. Busch, D. Mech, R. S. Patel, J. S. Sangwai, Effect of silica sand size on the formation kinetics of CO_2 hydrate in porous media in the presence of pure water and seawater relevant for CO_2 sequestration, J. Pet. Sci. Eng. 122 (2014) 1-9.
[146] M. Zi, D. Chen, G. Wu, Molecular dynamics simulation of methane hydrate formation on metal surface with oil, Chem. Eng. Sci. 191 (2018) 253-261.
[147] C. Cuadrado-Collados, J. Farrando-Pérez, M. Martínez-Escandell, L. A. Ramírez-Montoya, J. A. Menéndez, A. Arenillas, M. A. Montes-Morán, J. Silvestre-Albero, Well-defined meso/macroporous materials as a host structure for methane hydrate formation: Organic versus carbon xerogels, Chem. Eng. J. 402 (2020) 126276.
[148] A. Perrin, A. Celzard, J. F. Maréché, G. Furdin, Methane storage within dry and wet active carbons: A comparative study, Energy Fuels 17 (2003) 1283-1291.
[149] M. J. D. Mahboub, A. Ahmadpour, H. Rashidi, Improving methane storage on wet activated carbons at various amounts of water, J. Fuel Chem. Technol. 40 (2012) 385-389.
[150] X. Liu, D. Liu, W. Xie, X. Cui, Y. Chen, Methane hydrate uptake of mcm-41 mesoporous molecular sieves with preadsorbed water, J. Chem. Eng. Data 63 (2018) 1767-1772.
[151] C. Chen, Y. Li, J. Cao, Methane hydrate formation in hollow ZIF-8 nanoparticles for improved methane storage capacity, Catalysts 12 (2022) 1-13.
[152] L. Zhou, X. Liu, Y. Sun, J. Li, Y. Zhou, Methane sorption in ordered mesoporous silica SBA-15 in the presence of water, J. Phys. Chem. B. 109 (2005) 22710-22714.
[153] V. V. Koryakina, E. Y. Shitz, Usage of the Kolmogorov−Johnson−Mehl−Avrami model for the study of the kinetics of the formation of natural gas hydrate in inverse oil emulsions, Condensed Matter and Interphases 22 (2020) 327-335.

[154] B. L. L. D. Silva, I. L. Ferraz, D. F. do Nascimento, J. A. de Castro, L. Vitorazi, Sodium alginate polymer as a kinetic inhibitor of methane hydrate formation, J. Mater. Res. Technol. 12 (2021) 1999-2010.
[155] A. A. Aziz, S. A. Samsudin, J. N. Hay, M. J. Jenkins, The effect of a secondary process on polymer crystallization kinetics – 3. Co-poly (lactic acid), Eur. Polym. J. 94 (2017) 311-321.
[156] T. Kitajima, N. Ohtsubo, S. Hashimoto, T. Makino, D. Kodama, K. Ohgaki, Study on prompt methane hydrate formation derived by addition of ionic liquid, Am. Chem. Sci. J. 2 (2012) 100-110.
[157] J. J. Rivera, K. C. Janda, Ice particle size and temperature dependence of the kinetics of propane clathrate hydrate formation, J. Phys. Chem. C 116 (2012) 19062-19072.
[158] M. T. Nguyen, J. Amtawong, K. Smoll, A. Chanez, M. Yamano, H. G.-B. Dinh, S. Sengupta, R. W. Martin, K. C. Janda, Gas flow rate and temperature dependence of the kinetics of difluoromethane clathrate hydrate formation from CF_2H_2 gas and ice particles, J. Phys. Chem. C 120 (2016) 8482-8489.
[159] J. Amtawong, S. Sengupta, M. T. Nguyen, N. C. Carrejo, J. Gu, E. B. Fleischer, R. W. Martin, K. C. Janda, Kinetics of trifluoromethane clathrate hydrate formation from CHF_3 gas and ice particles, J. Phys. Chem. A 121 (2017) 7089-7098.
[160] R. M. Barrer, D. J. Ruzicka, Non-stoichiometric clathrate compounds of water. part 4.—kinetics of formation of clathrate phases, Trans. Faraday Soc. 58 (1962) 2262-2271.
[161] P.-C. Chen, W.-L. Huang, L. A. Stern, Methane hydrate synthesis from ice: influence of pressurization and ethanol on optimizing formation rates and hydrate yield, Energy Fuels 24 (2010) 2390-2403.
[162] E. Urbanovici, H. A. Schneider, H. J. Cantow, Some considerations concerning the temperature dependence of the bulk crystallization rate constants of polymeric materials, J. Polym. Sci., Part B: Polym. Phys. 35 (1997) 359.
[163] M. J. Hargis, B. P. Grady, Effect of sample size on isothermal crystallization measurements performed in a differential scanning calorimeter: A method to determine avrami parameters without sample thickness effects, Thermochim. Acta 443 (2006) 147-158.
[164] P. T. Kiss, A. Baranyai, A systematic development of a polarizable potential of water, J. Chem. Phys. 138 (2013) 204507.
[165] P. Paricaud, M. Predota, A. A. Chialvo, P. T. Cummings, From dimer to condensed phases at extreme conditions: accurate predictions of the properties of water by a gaussian charge polarizable model, J. Chem. Phys. 122 (2005) 244511-244514.
[166] C. Vega, J. L. Abascal, I. Nezbeda, Vapor-liquid equilibria from the triple point up to the critical point for the new generation of TIP4P-like models: TIP4P/Ew, TIP4P/2005, and TIP4P/ice, J. Chem. Phys. 125 (2006) 034503-034509.
[167] M. W. Mahoney, W. L. Jorgensen, A five-site model for liquid water and the reproduction of the density anomaly by rigid, nonpolarizable potential functions, J. Chem. Phys. 112 (2000) 8910-8922.
[168] H. Jiang, O. A. Moultos, I. G. Economou, A. Z. Panagiotopoulos, Hydrogen-bonding polarizable intermolecular potential model for water, J. phys. Chem. B 120 (2016) 12358-12370.
[169] T. R. Rettlch, Y. P. Hands, R. Battino, E. Wllhelm, Solubility of gases in liquids. 13. high-precision determination of henry's constants for methane and ethane in liquid water at 275 to 328 K J. Phys. Chem. 85 (1981) 3230-3237.
[170] H. Naghibi, S. F. Dec, S. J. Gill, Heat of solution of methane in water from 0 to 50 °C, J. Phys. Chem. 90 (1986) 4621-4623.